The Astrophysical Journal, 893:22 (21pp), 2020 April 10 https://doi.org/10.3847/1538-4357/ab7d39
© 2020. The Author(s). Published by the American Astronomical Society.
OPEN ACCESS

Electron Energy Partition across Interplanetary Shocks. III. Analysis

Lynn B. Wilson, III[1], Li-Jen Chen[1], Shan Wang[1,2], Steven J. Schwartz[3], Drew L. Turner[4], Michael L. Stevens[5], Justin C. Kasper[6], Adnane Osmane[7], Damiano Caprioli[8], Stuart D. Bale[9,10,11,12], Marc P. Pulupa[10], Chadi S. Salem[10], and Katherine A. Goodrich[10]

[1] NASA Goddard Space Flight Center, Heliophysics Science Division, Greenbelt, MD 20771, USA; lynn.b.wilsoniii@gmail.com
[2] Astronomy Department, University of Maryland, College Park, MD 20742, USA
[3] Laboratory for Atmospheric and Space Physics, University of Colorado, Boulder, Boulder, CO 80303, USA
[4] The Johns Hopkins University Applied Physics Laboratory, Laurel, MD 20723, USA
[5] Harvard-Smithsonian Center for Astrophysics, Harvard University, Cambridge, MA 02138, USA
[6] University of Michigan, Ann Arbor, School of Climate and Space Sciences and Engineering, Ann Arbor, MI 48109, USA
[7] Department of Physics, University of Helsinki, Helsinki, FI-00014, Finland
[8] Department of Astronomy and Astrophysics, University of Chicago, Chicago, IL 60637, USA
[9] Physics Department, University of California, Berkeley, CA 94720-7300, USA
[10] Space Sciences Laboratory, University of California, Berkeley, CA 94720-7450, USA
[11] The Blackett Laboratory, Imperial College London, London, SW7 2AZ, UK
[12] School of Physics and Astronomy, Queen Mary University of London, London E1 4NS, UK
Received 2020 February 7; revised 2020 March 4; accepted 2020 March 4; published 2020 April 9

Abstract

An analysis of model fit results of 15,210 electron velocity distribution functions (VDFs), observed within ±2 hr of 52 interplanetary (IP) shocks by the Wind spacecraft near 1 au, is presented as the third and final part on electron VDFs near IP shocks. The core electrons and protons dominate in the magnitude and change in the partial-to-total thermal pressure ratio, with the core electrons often gaining as much or more than the protons. Only a moderate positive correlation is observed between the electron temperature and the kinetic energy change across the shock, while weaker, if any, correlations were found with any other macroscopic shock parameter. No VDF parameter correlated with the shock normal angle. The electron VDF evolves from a narrowly peaked core with flaring suprathermal tails in the upstream to either a slightly hotter core with steeper tails or much hotter flattop core with even steeper tails downstream of the weaker and strongest shocks, respectively. Both quasi-static and fluctuating fields are examined as possible mechanisms modifying the VDF, but neither is sufficient alone. For instance, flattop VDFs can be generated by nonlinear ion acoustic wave stochastic acceleration (i.e., inelastic collisions), while other work suggested they result from the combination of quasi-static and fluctuating fields. This three-part study shows that not only are these systems not thermodynamic in nature; even kinetic models may require modification to include things like inelastic collision operators to properly model electron VDF evolution across shocks or in the solar wind.

Unified Astronomy Thesaurus concepts: Solar wind (1534); Interplanetary shocks (829); Solar coronal mass ejections (310); Solar coronal mass ejection shocks (1997); Space plasmas (1544); Plasma astrophysics (1261); Plasma physics (2089); Interplanetary particle acceleration (826)

1. Background and Motivation

Despite its collisionless, non-equilibrium nature, the existence of shock waves is still possible in the solar wind due to solar drivers (e.g., coronal mass ejections and/or corotating interaction regions) called interplanetary (IP) shocks (e.g., Gosling et al. 1993; Breneman et al. 2010; Aguilar-Rodriguez et al. 2011; Wilson et al. 2017), planetary bow shocks (e.g., Kellogg 1962; Wilson 2016), cometary bow shocks (e.g., Sagdeev et al. 1987), and nonlinearly steepened electromagnetic waves radiated by instabilities (e.g., Wilson et al. 2009, 2013). Even though the mean free path of a typical proton near 1 au can be nearly 1 au (i.e., orders of magnitude larger than the corresponding thermal gyroradii, ρ_{cp}, or inertial length, λ_p), the thickness of shock ramps—the spatial gradient scale length of the magnetic transition region—in the solar wind is often a few λ_e up to λ_p (e.g., Hobara et al. 2010; Mazelle et al. 2010). This is why shock waves in the solar wind, and in most astrophysical contexts, are called collisionless.

Collisionless shock ramp thickness is thought to depend upon macroscopic shock parameters like the Mach number (M_f), shock normal angle, θ_{Bn} (e.g., quasi-perpendicular shocks satisfy $\theta_{Bn} \geqslant 45°$), and upstream averaged plasma beta ($\langle\beta_{tot}\rangle_{up}$). Therefore, shocks in the solar wind/heliosphere are categorized by these parameters as being low (high) Mach number, $M_f \lesssim 2.5$ ($M_f > 2.5$), and low (high) beta shocks, $\beta_{up} \leqslant 1.0$ ($\beta_{up} > 1.0$; e.g., Sagdeev 1966; Coroniti 1970; Tidman & Krall 1971; Kennel et al. 1985; Wilson et al. 2017).

There are several key unresolved questions about the microphysical processes that regulate the dynamics of collisionless shock waves. One of the biggest outstanding problems in shock physics is the partition of energy between electrons and ions. A significant obstacle is that the mechanisms depositing/transferring energy are not predicted to act homogeneously (i.e., they are energy- and pitch-angle-dependent and can be species-dependent; e.g., Sagdeev 1966; Artemyev et al. 2013, 2014, 2015, 2016, 2017a, 2017b, 2018). Evidence supporting this prediction has been reported in some

Original content from this work may be used under the terms of the Creative Commons Attribution 4.0 licence. Any further distribution of this work must maintain attribution to the author(s) and the title of the work, journal citation and DOI.

case study observations at IP shocks (e.g., Wilson et al. 2009, 2010, 2012, 2013) and the terrestrial bow shock (e.g., Wilson et al. 2014a, 2014b; Oka et al. 2017, 2019; Chen et al. 2018; Goodrich et al. 2018, 2019). Further, most collisionless shocks are subsonic to electrons, yet electrons still behave as if they have experienced a shock, even showing Mach number–dependent effects (e.g., Feldman et al. 1982, 1983a, 1983b; Thomsen et al. 1985, 1987, 1993; Wilson et al. 2010; Masters et al. 2011). The question remains: How does a collisionless shock transform the bulk flow kinetic energy into other forms like electron and/or ion heating?

To determine the energy transfer mechanism, several previous studies examined the change in average electron temperature, $\Delta\bar{T}_{e,\mathrm{tot}}$ (see Appendix A for definitions), or the ratio of downstream-to-upstream average electron temperature, $\bar{R}_{Te,\mathrm{tot}}$, across the shock. These parameters were compared with the upstream average fast Mach number, $\langle M_f\rangle_{\mathrm{up}}$; the upstream average kinetic energy, $\langle|KE_{\mathrm{shn}}|\rangle_{\mathrm{up}}$; the change in the shock normal speed, $\Delta\bar{U}_{\mathrm{shn}}$; and the square of the shock normal speed, $\Delta\bar{U}^2_{\mathrm{shn}}$, and/or the change in kinetic energy across the shock.[13]

Feldman et al. (1983a) found weak, positive correlation between $\bar{R}_{Te,\mathrm{tot}}$ and $\langle M_f\rangle_{\mathrm{up}}$ (technically it was with $\langle M_{\mathrm{ms}}\rangle_{\mathrm{up}}$). Feldman et al. (1983c) found weak, positive linear relationships between both $\Delta\bar{T}_{e,\mathrm{tot}}$ and $\Delta\bar{T}_{p,\mathrm{tot}}$ and $\Delta\bar{U}_{\mathrm{shn}}$. Thomsen et al. (1987) examined electron heating at Earth's bow shock, finding a correlation between $\Delta\bar{T}_{e,\mathrm{tot}}$ and $\Delta\bar{U}^2_{\mathrm{shn}}$ with a few to ~10% of the kinetic energy transforming into electron heating. Later Schwartz et al. (1988) found a correlation between $\Delta\bar{T}_{e,\mathrm{tot}}$ and $\Delta\bar{U}^2_{\mathrm{shn}}$. They also show a strong, positive correlation for $\Delta\bar{T}_{e,\mathrm{tot}}$ versus $\Delta\bar{T}_{i,\mathrm{tot}}$, with a slope of ~0.2 and y-intercept of ~8.6 eV. Thomsen et al. (1993) examined ion and electron heating at the low Mach number, quasi-parallel Earth's bow shock, finding that ~6% of $\Delta\overline{KE}_{\mathrm{shn}}$ was converted to electron heating. Hull et al. (2000) found a positive, linear relationship between $\Delta\bar{T}_{e,\mathrm{tot}}$ and $\Delta\overline{KE}_{\mathrm{shn}}$ with a slope of $0.057^{+0.0041}_{-0.0039}$ (i.e., ~6% of of $\Delta\overline{KE}_{\mathrm{shn}}$ was converted to electron heating). Fitzenreiter et al. (2003) also found a linear relationship between $\Delta\bar{T}_{e,\mathrm{tot}}$ and $\Delta\bar{U}^2_{\mathrm{shn}}$. Finally, Masters et al. (2011) examined electron heating at the Kronian bow shock, finding that for most crossings, ~3%–7% of $\langle KE_{\mathrm{shn}}\rangle_{\mathrm{up}}$ was converted to electron heating. Thus, previous work suggests that the change in bulk flow kinetic energy should be correlated with the increase in temperature. Note that previous work has either inferred (e.g., Ghavamian et al. 2007, 2014) or showed with in situ measurements that stronger shocks heat ions more than electrons (e.g., Schwartz et al. 1988; Thomsen et al. 1993; Masters et al. 2011), with the fraction of electron heating varying with an inverse Mach number.[14] The inverse Mach number dependence was also found to be a piecewise distribution where ~50% of the total heating goes to electrons at low Mach number and changes to $\lesssim$10% at higher Mach number.

In this final part (Paper III) of this three-part study, the analysis of the fit results to the multi-component electron VDF analysis will be discussed in the context of the macroscopic shock parameters and some instability analysis. The results are summarized for the 52 IP shocks observed by the Wind spacecraft. The notation, symbols, and data sets used herein are the same as those in Wilson et al. (2019a; hereafter referred to as Paper I) and Wilson et al. (2019b; hereafter referred to as Paper II). Paper I discussed the methodology and described the data product resulting from the application of the fit software, and Paper II summarized the statistics of the fit results. This work will provide the physical analysis and interpretation of the results in the context of macroscopic shock parameters and some instability analysis.

2. Data Sets and Methodology

As in Papers I and II, all data are observed by instruments on the Wind spacecraft (Harten & Clark 1995) near 1 au. The data used herein include quasi-static magnetic field vectors ($\boldsymbol{B}_o$) from Wind/MFI (Lepping et al. 1995), electron and ion velocity distribution functions (VDFs) from Wind/3DP (Lin et al. 1995), and proton and alpha-particle velocity moments from the Wind/SWE Faraday Cups (Kasper et al. 2006; Ogilvie et al. 1995). The instrument details are described in Paper I. Parameters described with respect to $\boldsymbol{B}_o$ are in a field-aligned coordinate basis using a subscript j to denote the parallel ($j = \|$), the perpendicular ($j = \perp$), and total ($j = \mathrm{tot}$) directions. All electron parameters are shown with a subscript s denoting the component (or subpopulation) of the entire distribution, where $s = ec$ for the core, $s = eh$ for the halo, $s = eb$ for the beam/strahl, and $s = e$ for the entire distribution. The combined or mixed parameters (e.g., $\beta_{\mathrm{eff},j}$) use the subscripts $s = \mathrm{eff}$ for effective and $s = \mathrm{int}$ for integrated parameters (see Appendix A for definitions). The analysis of the VDFs presented herein was found within ±2 hr of 52 IP shocks found in the Wind shock database from the Harvard Smithsonian Center for Astrophysics[15] between 1995 February 26 and 2000 February 20 (for a full list of event dates and times, see the PDF file included with the additional supplemental material found at https://doi.org/10.5281/zenodo.2875806; Wilson et al. 2019c). The IP shocks examined were limited to fast-forward shocks that had burst mode electron VDFs within the chosen time range about each shock.

As in Paper II, the VDF results presented herein are relative to all 15,210 VDFs examined. The VDF fit results are taken from additional supplemental material in the form of two ASCII files (discussed in Paper II and described in Paper I; Wilson et al. 2019c). Of this total, 14,418 had stable model fits ($f^{(\mathrm{core})}$) for the core, 13,660 stable model fits ($f^{(\mathrm{halo})}$) for the halo, and 11,578 stable model fits ($f^{(\mathrm{beam})}$) for the beam/strahl. Note that all statistics presented herein are for stable fits with a fit flag for the respective component of two or higher. The selection justification of the VDFs are provided in Paper II. Similarly, this work follows Paper II with the following selection criteria:

1. *Criteria AT:* All VDFs satisfying: Fit Flag $\{c, h, b\} \geqslant 2$ and no violation of post-fit constraints
2. *Criteria UP:* All VDFs satisfying *Criteria AT* that were observed upstream of the IP shock ramp
3. *Criteria DN:* All VDFs satisfying *Criteria AT* that were observed downstream of the IP shock ramp
4. *Criteria LM:* All VDFs satisfying *Criteria AT* that were observed near IP shocks satisfying $\langle M_f\rangle_{\mathrm{up}} < 3$

[13] Some studies explicitly calculated the change in kinetic energy across the shock, $\Delta\overline{KE}_{\mathrm{shn}}$, while others only calculated $\Delta\bar{U}^2_{\mathrm{shn}}$.

[14] However, more complete analysis of astrophysical shocks that include neutral return currents found that the electron-to-ion temperature ratio cannot be constrained by Mach number (e.g., Blasi et al. 2012).

[15] https://www.cfa.harvard.edu/shocks/wi_data/

5. *Criteria HM:* All VDFs satisfying *Criteria AT* that were observed near IP shocks satisfying $\langle M_f \rangle_{up} \geqslant 3$
6. *Criteria PE:* All VDFs satisfying *Criteria AT* that were observed near IP shocks satisfying $\theta_{Bn} > 45°$
7. *Criteria PA:* All VDFs satisfying *Criteria AT* that were observed near IP shocks satisfying $\theta_{Bn} \leqslant 45°$

Superposed epoch analysis (SEA) of every fit parameter has been performed where the time stamps of each VDF are redefined as offsets from the associated IP shock ramp center time. Finally, to quantify the partition of energy for each component, all permutations of the difference (and ratio) between the upstream and downstream values are computed. Again, the value used for each shock is the median, and the uncertainty is half the magnitude of the difference between $X_{5\%}$ and $X_{95\%}$. The results were fit to model functions (e.g., power law), with the dependent variable/abscissa being the different macroscopic shock parameters. All permutations are used to avoid the subjectivity introduced by selecting a user-defined time period that serves as the upstream and downstream regions. The median was used instead of an average because again the data are normally distributed and the median is less influenced by large deviations/tails. The differences or ratios are then fit to a model function using both Poisson and Gaussian weights to find the best fit results.

Finally, it should be noted that the total time range (i.e., ± 2 hr) about each shock ramp is larger than the typical time range examined (i.e., ± 10 s of minutes). The purpose is ensure that the upstream analysis includes data that are not part of the electron foreshock. The extent of the downstream is defined purely to maintain symmetry about the shock ramp center. Although the analysis presented herein only discusses differences and analysis of the VDF solutions for the entire time range, the same analysis was performed on limited time ranges about the shock ramp for comparison (not shown). Alteration of the time range about the shock ramp did not yield significant differences for most parameters examined.

3. Superposed Epoch Analysis

In the following subsections, multiple figures presenting SEA of the various fit parameters are presented. In all sections, the subscripts $s = ec$ is for the core, $s = eh$ for the halo, $s = eb$ for the beam/strahl, and $s =$ eff for the effective components.

The time stamps of each VDF are redefined as offsets from the associated IP shock ramp center time. The data are partitioned into 120 second time windows and then one-variable statistical analysis is performed on all data within. The time window center is shifted by 22 s (i.e., roughly the sample period of the 3DP instrument in survey mode), and then the analysis is repeated. In this way, the data can remain at their original sample time without affecting the magnitudes through the use of a re-gridding algorithm by averaging or interpolating data to a common set of time stamps.

For every partitioned time window, $\tilde{X}$ is used as the center line (shown as a red line in Figures 1 and 2), $X_{5\%}$ is used as the lower line (shown as the lower cyan line in Figures 1 and 2), and $X_{95\%}$ is used as the upper line (shown as the upper cyan line in Figures 1 and 2). The median and percentile lines are then smoothed by selection criteria-dependent widths,[16] with *Criteria AT* smoothed over 10pts, *Criteria LM* smoothed over 20pts, *Criteria HM* smoothed over 30pts, *Criteria PA* smoothed over 30pts, and *Criteria PE* smoothed over 20pts. The data are also normalized by the upstream median values for each IP shock (see Tables 2–6 of additional supplemental material found in Wilson et al. 2020 for list of values) to remove relative offsets between any two IP shocks.

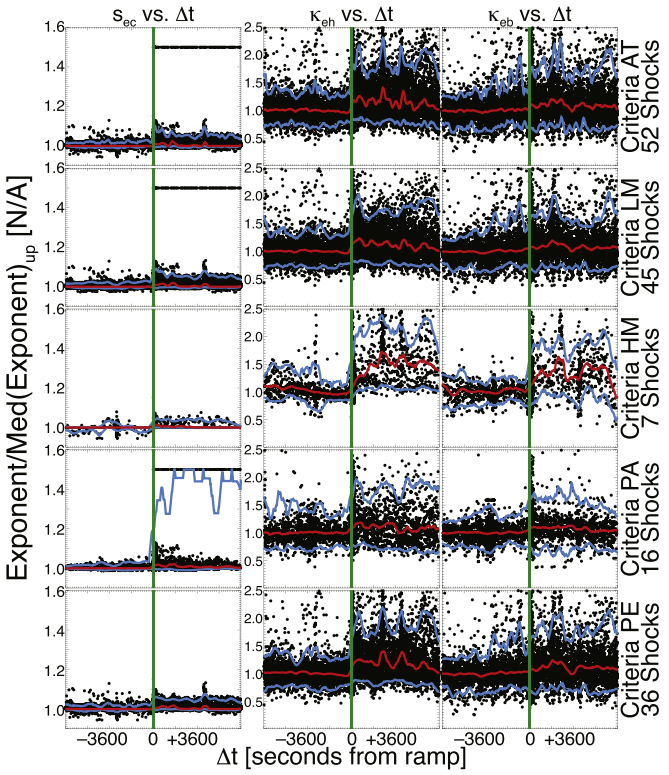


Figure 1. Superposed epoch analysis plot of the core, s_{ec}, halo, κ_{eh} (middle column), and beam/strahl, κ_{eb} (right column), exponents separated into *Criteria AT* (first row), *Criteria LM* (second row), *Criteria HM* (third row), *Criteria PA* (fourth row), and *Criteria PE* (fifth row). The red line shows the smoothed $\tilde{X}$ values of the partitioned data. The lower(upper) cyan lines are the smoothed $X_{5\%}(X_{95\%})$ values of the partitioned data. The vertical green line indicates the ramp center time. All data for a given IP shock are normalized by an upstream median value given in Wilson et al. (2020), table 5. Note that all panels share the same horizontal axis range, but the first column has a different vertical range than the latter two.

The median and percentiles used as the data are not normally distributed about a mean for each partitioned time window, as implied by the non-Gaussian histogram distributions shown in Paper II. The SEA plots provide the trend and typical ranges of the various parameters relative to the shock ramp center to illustrate changes. The parameters are also separated by the provided selection criteria to illustrate macroscopic shock parameter dependence.

3.1. Exponents

In this section, SEAs of $s_{ec}/\langle s_{ec} \rangle_{up}$, $\kappa_{eh}/\langle \kappa_{eh} \rangle_{up}$, and $\kappa_{eb}/\langle \kappa_{eb} \rangle_{up}$ are introduced and discussed in Figure 1 (see Appendix A for definitions). First, 50% of the halo and beam/strahl exponents (i.e., between the lower and upper quartiles) satisfy $3.57 \lesssim \kappa_{eh} \lesssim 5.31$ and $3.41 \lesssim \kappa_{eb} \lesssim 5.11$, which are consistent with previous solar wind observations near 1 au (e.g., Maksimovic et al. 1997, 2005; Štverák et al. 2009; Pierrard et al. 2016; Tao et al. 2016a, 2016b; Lazar et al. 2017; Horaites et al. 2018). (Note there are no studies with which to compare the s_{ec} values).

[16] As shown in Paper II, there are fewer fit results for *Criteria HM* than *Criteria LM*, and so larger smoothing windows were required.

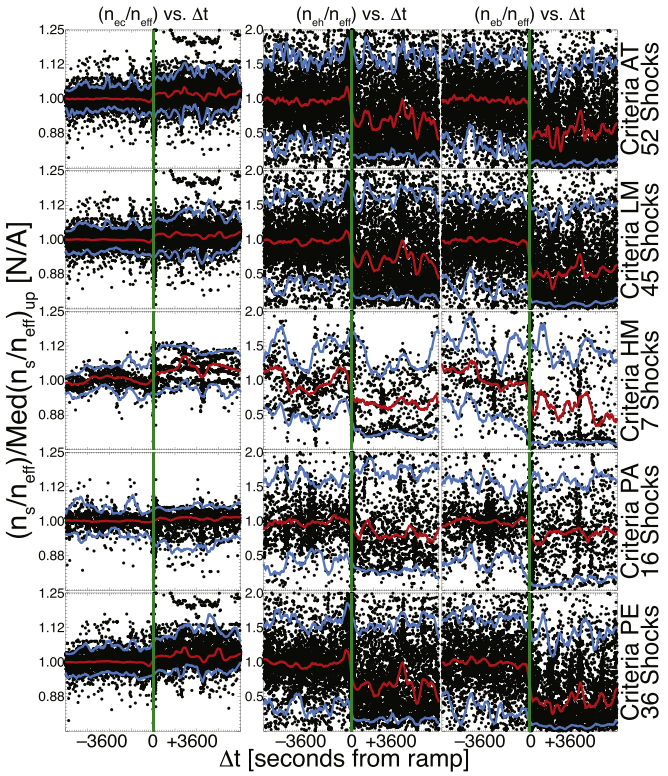


Figure 2. Superposed epoch analysis plot of the electron component density ratios $n_{ec}/n_{\rm eff}$ (left column), $n_{eh}/n_{\rm eff}$ (middle column), and $n_{eb}/n_{\rm eff}$ (right column). The normalization values for each IP shock are given in Wilson et al. (2020), Table B2. The format is the same as Figure 1.

The s_{ec} exponents are relatively constant across most IP shocks, with a few exceptions for *Criteria LM* and *Criteria PA* shocks showing values up near ∼1.5. The *Criteria HM* are especially sparsely populated in the downstream, as many of these VDFs were fit to the asymmetric self-similar model distribution (i.e., p_{ec} and q_{ec} exponents, not shown). However, the range of data between $X_{5\%}$ and $X_{95\%}$ is larger in the downstream, consistent with the interpretation of a wave-induced inelastic interaction discussed in Paper I.

The κ_{eh} panels (middle column) are more interesting and varied. For instance, the running median clearly increases across the shock. The change is the largest for *Criteria HM* and *Criteria PE* shocks. Theory and simulation suggest that stronger and more oblique shocks are better at energizing suprathermal electrons (e.g., Treumann 2009; Caprioli & Spitkovsky 2014; Park et al. 2015; Trotta & Burgess 2019). However, if the normalization used in Figure 1 is removed (not shown), the upstream only values of κ_{eh} between $X_{\rm min}$ and $X_{\rm max}$ cover a similar range for *Criteria LM* and *Criteria HM* shocks, with similar running medians as well. The downstream only κ_{eh} values are larger at *Criteria HM* than *Criteria LM* shocks, which explains the larger one-variable statistics values of κ_{eh} for *Criteria HM* than *Criteria LM* shocks shown in Paper I.

Note that the one-variable statistics of κ_{eh} reported in Paper I showed a slightly larger value for *Criteria PE* than *Criteria PA* shocks in agreement with the larger change across *Criteria PE* than *Criteria PA* shocks observed in Figure 1, consistent with theory and simulations (e.g., Wu 1984; Park et al. 2013; Trotta & Burgess 2019). While the change is not in the direction expected, the magnitude of the change is certainly larger for *Criteria HM* than *Criteria LM* shocks, suggesting stronger shocks have more of an impact on the halo than weaker. While the upstream kappa values have recently been predicted to increase with increasing Mach number for quasi-perpendicular shocks (Trotta & Burgess 2019), the normalization by the upstream median values for each shock removed the relative offsets to avoid this potentially misleading difference.

The increase in κ_{eh} across the shocks could result from several effects. For instance, it could result from core electrons being energized to suprathermal energies, initially starting with a larger equivalent kappa value, thus increasing the overall suprathermal exponent value. The increase in κ_{eh} could also result from acceleration through a quasi-static electric field (e.g., Scudder et al. 1986; Schwartz et al. 1988, 2011; Mitchell & Schwartz 2014; Schwartz 2014) for a one-dimensional VDF. The change in κ_{eh} for a two-dimensional VDF in velocity space is complicated if the quasi-static electric field is not uniformly aligned with both component directions in velocity space, as a kappa VDF is not a simple power law (e.g., Livadiotis 2015). Even so, the effect of a quasi-static electric field could result in the fit software finding a larger kappa value as the higher energy particles change velocity by a smaller fraction than the lower. However, the nonlinear relationship between the values of κ_s, n_s, and $V_{Ts,j}$ in affecting the shape and peak phase space density of a bi-kappa VDF (e.g., see Figure 2 of Paper I) makes it difficult to interpret the change in κ_{eh}.

The κ_{eb} panels (right-hand column) are less dynamic than the κ_{eh} panels, but there is an important similarity. The change in the running median is largest for *Criteria HM* shocks, with all other selection criteria showing little-to-no change or a weak gradual change across the entire time range. The biggest difference between κ_{eh} and κ_{eb} is that the latter does not show a clear increase at the shock ramp for *Criteria PE* shocks. Similar to the discussion above for κ_{eh}, if the normalization is removed from Figure 1 for κ_{eb}, the difference between *Criteria LM* and *Criteria HM* shocks is mostly in the variation in the running median. For *Criteria LM* shocks, the running median of κ_{eb} is very smooth and does not change much at the shock ramp (i.e., changes by less than ∼0.5), while the running median for *Criteria HM* shocks fluctuates with a normalized amplitude at or above unity. Again, the change in the running median does not show a strong change at the shock ramp in the unnormalized SEA (not shown).

3.2. Density Ratios

In this section, SEAs of $n_s/n_{\rm eff}$ are introduced and discussed, for the core ($s = ec$), halo ($s = eh$), beam/strahl ($s = eb$), and effective ($s = $ eff). The halo-to-effective density ratios are presented in the first column of Figure 2, the halo-to-effective ratios are presented in the second column, and the beam-to-effective ratios are presented in the third column.

Figure 2 shows the ratio of each electron component number density to the effective number density, $n_{\rm eff}$ (see Appendix A for definitions), to illustrate the relative change in the fractional composition of the electron distribution. That is, the SEA plots show whether the core, halo, and/or beam/strahl number density fraction increase or decrease across the shock for each selection criteria. It is quite obvious that the median core fraction always increases across the shock, regardless of selection criteria. The difference between selection criteria is that magnitude of the change (e.g., *Criteria PA*) shows very little positive change in the running median and a skewness toward smaller values in the running 5th percentile.

Unlike the core, both the halo and beam/strahl fractional densities decrease across the shock for all selection criteria. Again, the weakest change is found in the *Criteria PA* shocks, which is not surprising as quasi-parallel shocks show smaller magnetic field compression ratios. Thus, the change in the core density is smaller which impacts the halo and beam/strahl fits. The largest change across the shock ramp occurred for *Criteria LM* and *Criteria PE*. It should also be noted that the gradient in the running median is sharpest for the beam/strahl component. The halo shows a short enhancement upstream of the shock ramp and then a decrease that continues shortly into the downstream past the ramp. The width of the upstream enhancement is larger for the *Criteria HM* than *Criteria LM* shocks, suggesting it results from some form of shock acceleration forming an electron foreshock. This is further evidenced by the stark difference in the running median profile between the *Criteria PA* and *Criteria PE* shocks, where the latter are expected to be better at energizing electrons (e.g., Wu 1984; Park et al. 2013; Trotta & Burgess 2019).

The beam/strahl gradients occur almost entirely in the thin region focused on the ramp. On the timescale shown in these figures, one minor tick mark is ∼180 s, so the halo gradient from upstream to downstream lasts upward of ∼15 minutes. The beam/strahl gradient is much shorter at ∼6 minutes (except for *Criteria PA* and *Criteria HM* shocks, which have a much gentler gradient). Recall the time windows for calculating the running median are 120 s and the windows are shifted by 22 s each time; thus the sharpest gradient one might expect would be slightly surpassing 2 minutes.

These plots also show that the fraction of suprathermal particles decreases across most IP shocks, which may explain why the suprathermal exponents tend to increase across the shocks. Although the suprathermal temperatures tend toward larger values in the downstream regions (see additional SEA plots of $T_{s,j}$ found in Wilson et al. 2020), the change is very weak except for *Criteria HM* shocks. However, the core temperature changes across the shocks are much more dramatic than both the halo and beam/strahl. Further, the beam/strahl shows the weakest changes in $T_{s,j}$ for all selection criteria (i.e., the beam/strahl component's mean kinetic energy is not strongly affected by the shock).

3.3. Betas

This section provides superposed epoch analyses (SEAs) of the electron plasma betas, $\beta_{s,j}$, for the core ($s = ec$), halo ($s = eh$), and beam/strahl ($s = eb$) components. The core betas are presented in Figure 3, the halo temperatures are presented in Figure 4, and the beam/strahl temperatures are presented in Figure 5.

The next thing to examine is the plasma betas, $\beta_{s,j}$, for the core ($s = ec$), halo ($s = eh$), and beam/strahl ($s = eb$) components. The SEA plots in Figures 3–5 of $\beta_{s,j}$ show the largest change across the shock compared to all other electron fit parameters examined. Of the three components, the core shows the smallest change, but all three electron components decrease across the shock. The weak decrease in $\beta_{ec,j}$, compared to $\beta_{eh,j}$ and $\beta_{eb,j}$, is dominated by the increase in the magnitude of $\boldsymbol{B}_o$ across the shock, since both $T_{ec,j}$ and n_{ec} increase. Although both $T_{eh,j}$ and $T_{eb,j}$ tend to increase across the shock, the increase is weak. This weak increase coupled with the stronger decrease in both the fractional n_{eh} and n_{eb} and

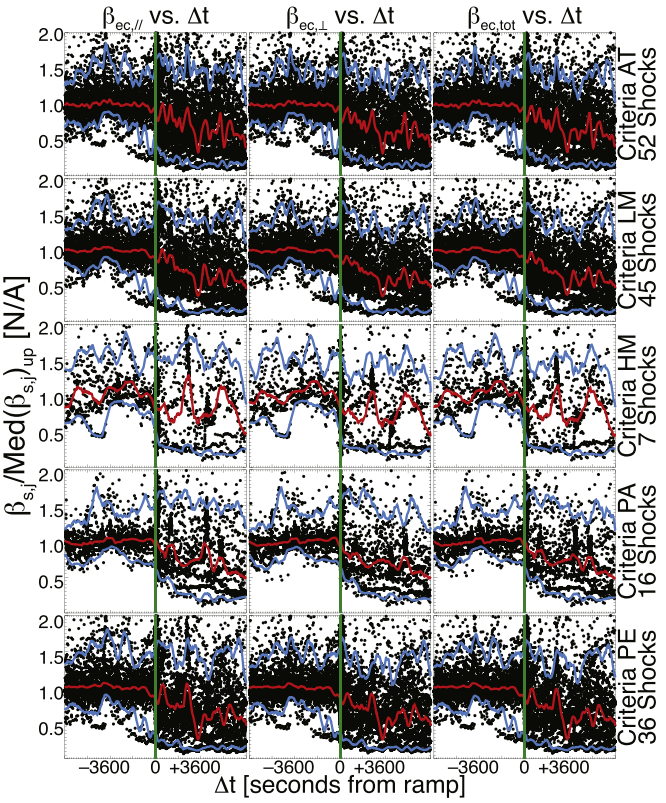


Figure 3. SEA plots of the core plasma betas $\beta_{ec,\parallel}$ (left column), $\beta_{ec,\perp}$ (middle column), and $\beta_{ec,\mathrm{tot}}$ (right column). The normalization values for each IP shock are given in Wilson et al. (2020), Table 4. The format is similar Figure 1, but all three columns share the same vertical axis scale.

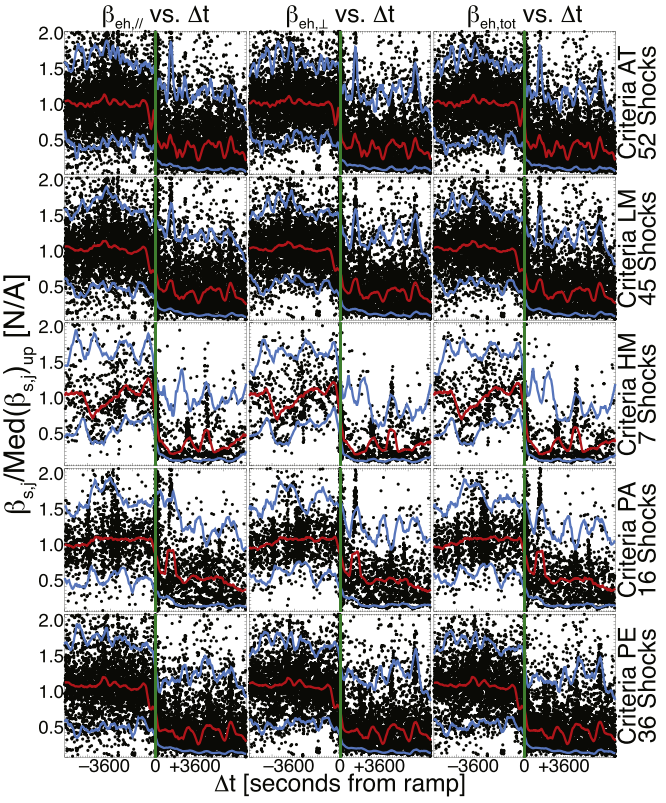


Figure 4. SEA plots of the halo plasma betas $\beta_{eh,\parallel}$ (left column), $\beta_{eh,\perp}$ (middle column), and $\beta_{eh,\mathrm{tot}}$ (right column). The normalization values for each IP shock are given in Wilson et al. (2020), Table 4. The format is the same as Figure 3.

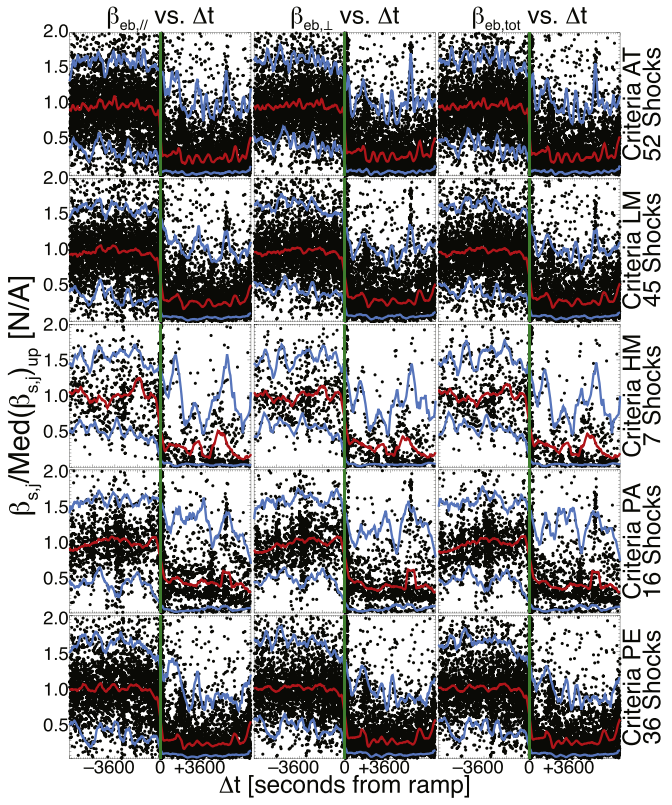


Figure 5. SEA plots of the beam/strahl plasma betas $\beta_{eb,\parallel}$ (left column), $\beta_{eb,\perp}$ (middle column), and $\beta_{eb,\mathrm{tot}}$ (right column). The normalization values for each IP shock are given in Wilson et al. (2020), Table 4. The format is the same as Figure 3.

increase in the magnitude of $\boldsymbol{B}_o$ makes for the corresponding decrease in suprathermal betas. Note, however, that the changes in n_{eff} and $\boldsymbol{B}_o$ are largely governed by the Rankine–Hugoniot conservation relations, while the change in any given $T_{s,j}$ is not. The change in $T_{ec,j}$ is due to the partition of free energy available due to $\Delta\overline{KE}_{\mathrm{shn}} \neq 0$, which will be discussed in Section 5.

Similar to the fractional n_{eh}, there is evidence of a foreshock in $\beta_{eh,j}$ shown as a two-step decrease—the beta begins to drop ahead of the shock ramp, reaches a plateau or slight jump near the ramp, then continues to drop to the downstream values for all selection criteria except *Criteria HM* and *Criteria PA*. The interesting thing is that the upstream running median is roughly near unity for all $\beta_{s,j}$, by design of course, but the downstream running median drops to as low as ∼0.20 for $\beta_{eh,j}$ and $\beta_{eb,j}$. That is, the running median decreases by upward of ∼80% across the shock for the suprathermal electrons. Therefore, the ratio of the thermal-to-magnetic field energy density of the suprathermal electrons is upward of ∼80% smaller in the downstream than upstream. Another interesting feature is that $\beta_{eh,j}$ begins to decrease upstream of the ramp center near the times when the fractional n_{eh} increases, which appears to be due to a local decrease in $T_{eh,j}$.

There is some bias in the steepness of the gradient due to the cluster of data near the ramp center of the IP shocks. This is due to the burst mode trigger of the 3DP instrument, which was designed to capture shock ramps in high time resolution. Thus, the large spread of values near the ramp center is dominating many of the running median calculations through that time period. In effect, this is actually reducing the variance in the running median seen in the more sparsely sampled far upstream and downstream regions. Therefore, it is worth noting to avoid overinterpreting these gradients.

4. Instability Analysis

In this section, numerical instability thresholds will be presented. The purpose of examining various instabilities is driven, in part, by the lack of dependence on many macroscopic shock parameters of the change in many electron fit parameters (as will be discussed in Section 5) and that waves radiated by instabilities often drive VDFs away from Maxwellians (e.g., they generate power laws and/or other non-Maxwellian features; Verscharen et al. 2018, 2019). There is also the motivation discussed in Paper I regarding the distribution of energy from a wave to the particles. The issue of inelasticity versus a more standard heating is discussed. Note that inelastic collisions have been tangentially discussed under different circumstances in previous theoretical work (e.g., Scudder & Olbert 1979). That is, inelastic scattering will increase the core exponents, s_{ec} or p_{ec} and q_{ec}, but may or may not cause a significant change in $T_{ec,j}$, while the standard idea of heating involves only the change in $T_{ec,j}$ without affecting the exponents.

Whether the core exponent changes or the temperature changes is critical for determining the change in the VDF profile/shape. For instance, whistler modes interacting with an initial Maxwellian VDF can generate strong deviations from Maxwellianity (e.g., Saito & Gary 2007; Gary et al. 2011; Chang et al. 2013; Hughes et al. 2014), typically resonating with the suprathermal halo and/or beam/strahl (e.g., Coroniti et al. 1982; Lengyel-Frey et al. 1994, 1996; Wilson et al. 2012, 2013; Oka et al. 2017, 2019). Whistler waves are also of interest because there is some observational evidence that they can generate energetic electron tails (e.g., Wilson et al. 2012, 2016; Oka et al. 2019). If the whistler is radiated by the whistler heat flux instability (WHFI; Gary et al. 1994, 1999; López et al. 2019; Shaaban et al. 2019b; Shaaban & Lazar 2020), during the radiation of the wave fields, the skewness of the VDF will reduce and the heat flux carrying electrons will scatter. The net effect will increase $\mathcal{A}_{eb}$. The wave fields can also pitch-angle scatter the halo electrons, resulting in larger $\mathcal{A}_{eh}$. If the whistler is radiated by the temperature anisotropy instability (WTAI), the act of radiating the wave fields will reduce $\mathcal{A}_{eh}$ and/or $\mathcal{A}_{eb}$. The waves can propagate to another location and pitch-angle scatter the suprathermal particles, which increases $\mathcal{A}_{eh}$ and/or $\mathcal{A}_{eb}$, much like the WHFI-driven waves.

Ion acoustic waves (IAWs) have been observed in the solar wind and near collisionless shocks for over 40 yr (e.g., Fredricks et al. 1968, 1970; Gurnett & Anderson 1977; Gurnett et al. 1979b; Kurth et al. 1979). They have been shown to be ubiquitous at collisionless shocks and of large amplitude (e.g., Wilson et al. 2007). They are thought to be driven by the free energy in currents (e.g., Biskamp et al. 1972; Lemons & Gary 1978), temperature gradients (e.g., Allan & Sanderson 1974), electron heat flux (e.g., Dum et al. 1980), or ion/ion-streaming instabilities (e.g., Akimoto et al. 1985; Akimoto & Winske 1985; Auer et al. 1971; Goodrich et al. 2019), or they can result from a nonlinear wave-wave process (e.g., Cairns & Robinson 1992; Dyrud & Oppenheim 2006; Kellogg et al. 2013; Saito et al. 2017). In the nonlinear stages of their evolution, they have been shown in simulations to cause strong deviations from

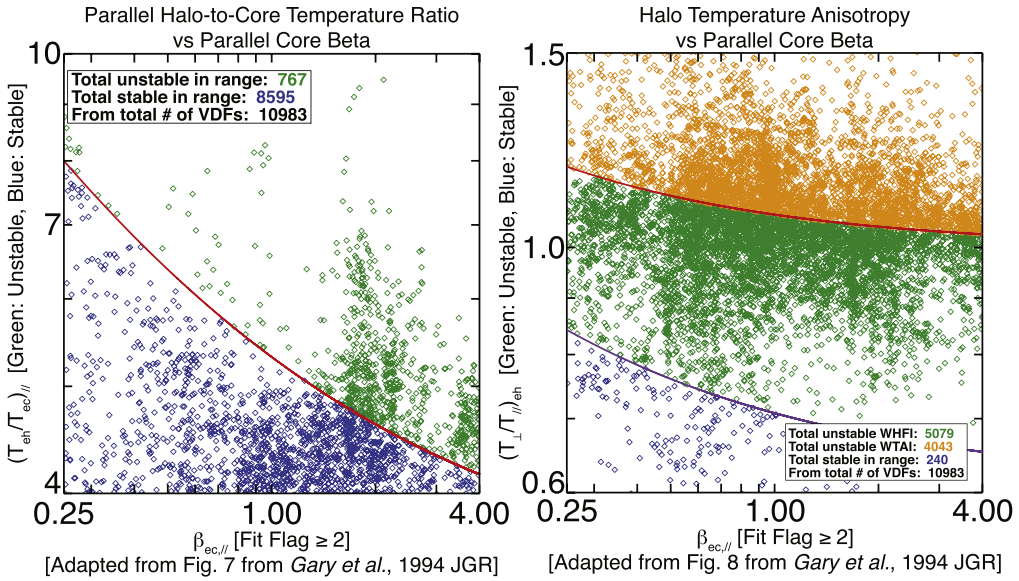


Figure 6. Adaptations of Figures 7 and 8 from Gary et al. (1994), showing the observed data from the current study against the calculated instability threshold for the whistler heat flux (WHFI) and temperature anisotropy (WTAI) instabilities as a function of $\beta_{ec,\parallel}$ for different $\mathcal{T}_{ec\parallel}^{eh}$ (left-hand panel) and $\mathcal{A}_{eh}$ (right-hand panel) values. Diamonds shown in green and orange are unstable while blue are stable. The red and purple lines are the numerical thresholds from the original figures corresponding to $\gamma_{max} > 10^{-1}\ \Omega_{cp}$.

Maxwellianity toward self-similar core electron VDFs, with s_{ec} or p_{ec} reaching values as large as 5 (e.g., Vedenov 1963; Sagdeev 1966; Dum et al. 1974; Dum 1975; Dyrud & Oppenheim 2006).

Note that the analysis presented in the following includes a larger than typical time range (i.e., ±2 hr) about the shock ramp. Therefore, some of the results may be more indicative of the solar wind than the shock itself. Further, the following analysis uses only the fit parameters from all the electron components and both the protons and alpha particles (Kasper et al. 2006) but does not directly include effects of non-Maxwellian features in any of the calculations. That is, the calculations use fit parameters, like density and temperature, directly in analytical formulas and numerical estimates for a given instability threshold without modification of the formula or numerical estimates. If the threshold involves only the total ion and electron populations, then the effective electron and total ion parameters are used.

4.1. Whistler Instabilities

In this section, the instability thresholds for the WHFI and WTAI are examined based on the observed properties of the electron VDFs. Specifically, this section will focus on the numerical results of Gary et al. (1994) and Gary et al. (1999). To this end, the electron heat flux is calculated, which requires stable fit solutions for all three electron components (i.e., 10,983 of the total 15,210 VDFs examined satisfy this requirement; see Paper II for further details on the integration of the total electron model functions).

Figure 6 is an adaptation of Figures 7 and 8 from Gary et al. (1994), where the red (purple) line in the left (right) panel corresponds to the lower line in Figure 7(8) of the original work (i.e., the threshold for the WHFI). The threshold values shown in Figure 6 are defined as instabilities having a maximum positive growth rate, γ_{max}, satisfying $\gamma_{max} > 10^{-1}\ \Omega_{cp}$. Over-plotted are the electron VDF fit results from the present work. In the range of $\beta_{ec,\parallel}$ shown, there are 9362 valid VDF fit results. For reference, 90% of the data for *Criteria AT* satisfy the following:

1. $0.28\ \mathrm{rad\ s^{-1}} \lesssim \Omega_{cp} \lesssim 2.03\ \mathrm{rad\ s^{-1}}$;
2. $0.49\ \mathrm{s} \lesssim \Omega_{cp}^{-1} \lesssim 3.52\ \mathrm{s}$;
3. $0.76\ \mathrm{km} \lesssim \rho_{ceff} \lesssim 4.04\ \mathrm{km}$;
4. $23.6\ \mathrm{km} \lesssim \rho_{ceff} \lesssim 167\ \mathrm{km}$;
5. $0.93\ \mathrm{km} \lesssim \lambda_{ceff} \lesssim 3.65\ \mathrm{km}$; and
6. $36.7\ \mathrm{km} \lesssim \rho_{ceff} \lesssim 154\ \mathrm{km}$.

Thus, the growth times corresponding to the threshold lines in Figure 6 satisfy $4.92\ \mathrm{s} \lesssim \gamma_{max}^{-1} \lesssim 35.2\ \mathrm{s}$ or ∼0.03%–0.24% of the total time examined around each IP shock.

Figure 6 shows that >80% of all 10,983 VDFs are at or above the threshold for either the WHFI or WTAI. Limiting to the 9362 VDFs shown in Figure 6, ∼54% are unstable to the WHFI and ∼43% are unstable to the WTAI. That is, only ∼3% of the VDFs are stable for these criteria. Further, Gary et al. (1999) noted that in the presence of a finite electron heat flux and $\mathcal{A}_{eh} > 1.01$, the heat flux carrying electrons are always unstable to the WHFI.[17] Of the 10,983 VDFs with a calculated heat flux, ∼62% satisfied $\mathcal{A}_{eh} > 1.01$ (i.e., ∼62% are at least linearly unstable to the WHFI). These rates are significantly larger than recent work using data from the ARTEMIS mission (e.g., Tong et al. 2019), which found occurrence rates of whistler waves to be $\lesssim$2%. However, the ARTEMIS work limited the observations to the pristine solar wind and used $\mathcal{A}_{\mathrm{eff}}$ instead of $\mathcal{A}_{eh}$ for anisotropy threshold calculations. When they limit their occurrence rate estimates to intervals satisfying $\mathcal{A}_{\mathrm{eff}} > 1$, the rates jump to ∼15%.

Note that Gary et al. (1994) only used two bi-Maxwellian electron components while this work uses three non-Maxwellian electron components, which makes the comparison subject to scrutiny. For instance, the use of bi-Maxwellian instead of bi-kappa is known to cause differences in the WHFI (e.g., Shaaban et al. 2018; Lee et al. 2019) and other instabilities

[17] There is the additional criteria that $\beta_{ec,\parallel} > 0.25$ is included in this discussion, but this is already imposed on the data presented in Figure 6.

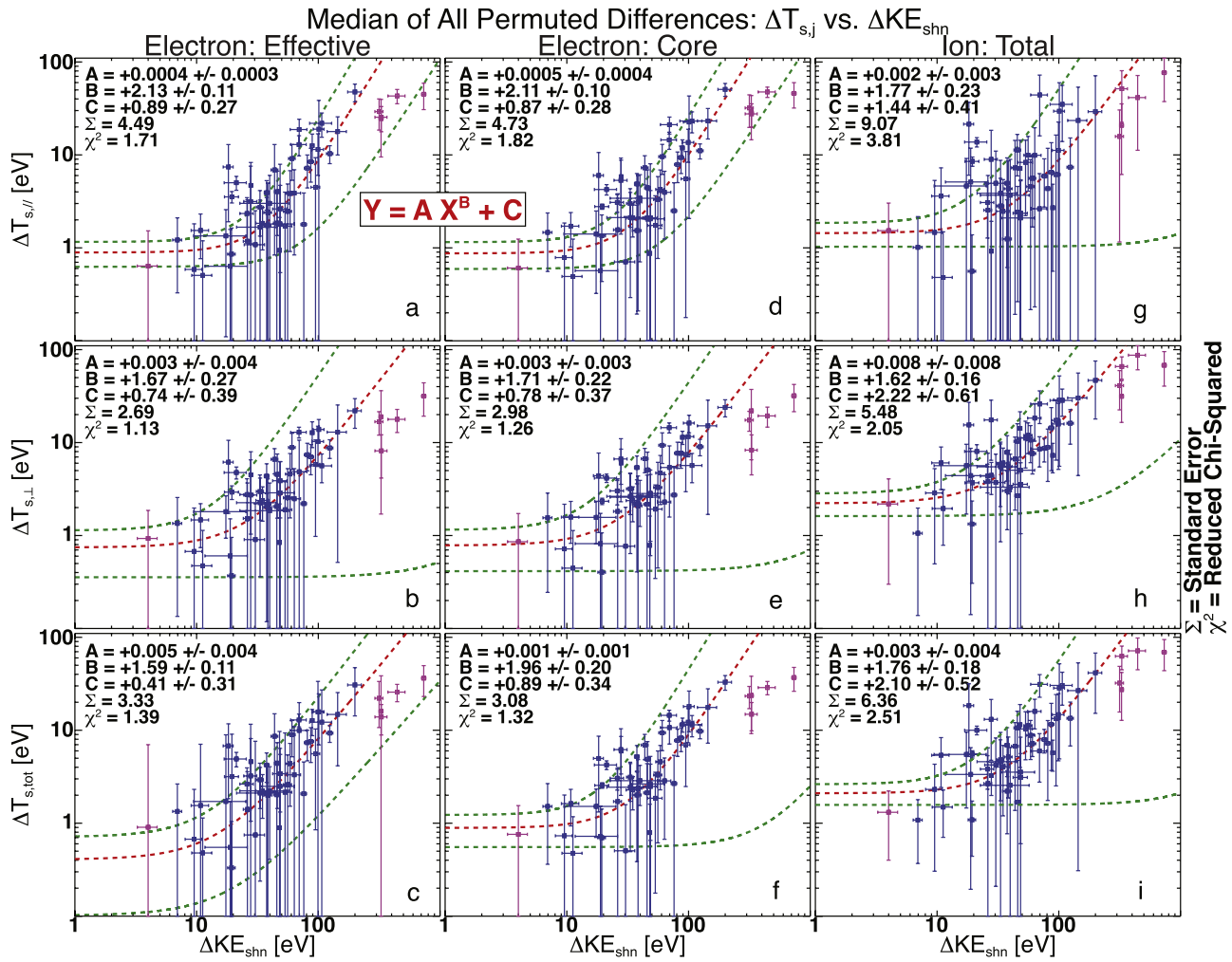


Figure 7. Median of the permuted temperature differences, $\widetilde{\Delta T}_{s,j}$, vs. the change in shock kinetic energy, $\Delta\overline{KE}_{\rm shn}$ [eV], for the effective electron temperatures (first column), core electron temperatures (second column), and total ion temperatures (third column). The first, second, and third rows show the parallel, perpendicular, and total temperature changes, respectively. The red dashed line in every panel is a power-law fit (function defined between panels (a) and (d)) to the data and the green lines show the associated uncertainty bounds. The associated fit parameters are shown in each panel. The magenta colored points were ignored during the fit process as outliers.

(e.g., Lazar et al. 2012, 2013, 2014, 2017, 2018, 2019; Shaaban et al. 2019a). In addition, the definition of $\mathcal{T}_{ec\|}^{eh}$ used to create the left-hand panel in Figure 6 relied upon the halo and core components only, not a single suprathermal population like that used by Gary et al. (1994).

More than half of the VDFs are unstable to the WHFI, which is consistent with the observation that both $\mathcal{A}_{eb}$ and κ_{eb} are generally smaller than $\mathcal{A}_{eh}$ and κ_{eh} (see Paper II for values and statistics), respectively. That is, the radiation of the wave reduces $\mathcal{A}_{eb}$ and κ_{eb} and subsequent scattering can increase $\mathcal{A}_{eh}$, though it should be noted that $\kappa_{eh} \gtrsim \kappa_{eb}$ has been found to be true in previous solar wind studies. Statistically, the halo exponent tends to be larger than the beam/strahl at 1 au in some studies (e.g., Štverák et al. 2009), though others show the converse and a solar cycle dependence (e.g., Tao et al. 2016a). Therefore, the larger κ_{eh} may be a remnant of the typical conditions in the solar wind and not directly related to local instabilities. Alternately, the differences between the two exponents may be observed with this relationship precisely because the two populations are intrinsically coupled through whistler-like instabilities. It may also be that quasi-static fields are affecting the core more than the halo by energizing them to suprathermal energies, thus effectively increasing the suprathermal electron exponents (e.g., Scudder et al. 1986; Schwartz et al. 1988, 2011; Mitchell & Schwartz 2014; Schwartz 2014). Kinetic simulations are required to resolve this discrepancy and are beyond the scope of this study.

4.2. Other Instabilities

In this section, the instability thresholds for short wavelength,[18] electrostatic IAWs will be calculated and discussed. The purpose is to calculate the probability of occurrence and determine whether such modes could be playing a role in the evolution of the electron VDFs across the examined IP shocks.

A long-standing problem in solar wind physics is the occurrence of short wavelength IAWs (e.g., Fuselier & Gurnett 1984; Gurnett et al. 1979a, 1979b; Wilson et al. 2007) despite the commonly observed electron-to-ion temperature ratios satisfying $\mathcal{T}_i^{\rm eff}{}_{\rm tot} < 3$. The temperature ratio threshold derives from the assumption of single, isotropic Maxwellian VDFs for both the electrons and ions, which shows that current-driven

[18] *Short* here implies $\lambda/\lambda_{De} \sim 2\pi$ to more than several 10 s (i.e., not the large wavelength limit sometimes called the *slow ion acoustic mode*).

IAWs are heavily Landau damped if $\mathcal{T}_{i\,\mathrm{tot}}^{\mathrm{eff}} < 3$ (e.g., Fried & Gould 1961; Fried & Wong 1966; Gould 1964; Gurnett et al. 1979a). However, temperature gradients (e.g., Priest & Sanderson 1972; Allan & Sanderson 1974; Dum 1978a, 1978b), shear flow (e.g., Agrimson et al. 2001; Gavrishchaka et al. 1999), nonlinear whistler wave decay (e.g., Saito et al. 2017), finite electron heat flux (e.g., Dum et al. 1980), nonlinear Langmuir wave decay (e.g., Zakharov 1972; Zakharov & Rubenchik 1972; Kellogg et al. 2013; Cairns & Layden 2018), and ion-ion instabilities (e.g., Ashour-Abdalla & Okuda 1986; Winske et al. 1987; Goodrich et al. 2018, 2019) have all been shown to reduce or eliminate this temperature ratio threshold.

Regardless, the occurrence rates of $\mathcal{T}_{p\,j}^{ec} \geqslant 3$ and $\mathcal{T}_{p\,j}^{\mathrm{eff}} \geqslant 3$ were calculated for reference. For *Criteria AT*, $\mathcal{T}_{p\,j}^{ec} \geqslant 3$ is satisfied for ∼29.5%, ∼22.6%, and ∼24.4% of the VDFs for $j = \parallel, \perp$, and tot, respectively. These occurrence rates jump to ∼34.8%, ∼27.2%, and ∼28.6% for $\mathcal{T}_{p\,j}^{\mathrm{eff}} \geqslant 3$. If the data are limited to *Criteria UP*, the occurrence rates for $\mathcal{T}_{p\,j}^{ec} \geqslant 3$ increase to ∼38.2%, ∼38.2%, and ∼37.7%, and similarly the rates for $\mathcal{T}_{p\,j}^{\mathrm{eff}} \geqslant 3$ also increase to ∼47.4%, ∼46.1%, and ∼42.8%. If the time range is limited to $-120\,\mathrm{s} \leqslant \Delta t \leqslant +3\,\mathrm{s}$ (where Δt is the time from ramp center), the rates for $\mathcal{T}_{p\,j}^{\mathrm{eff}} \geqslant 3$ are ∼41.2%, ∼32.3%, and ∼26.4%. Thus, even if the analysis is limited to times near the shock ramps, the occurrence rates of temperature ratios meeting or exceeding three are smaller than all upstream observations. The occurrence rate of IAWs has been shown to peak within collisionless shock ramps (e.g., Fuselier & Gurnett 1984; Wilson et al. 2007, 2014a, 2014b; Goodrich et al. 2018; Cohen et al. 2019; Davis et al. 2020), and this rate was found to be independent of $\mathcal{T}_{p\,\mathrm{tot}}^{e}$ (e.g., Wilson et al. 2007). That the rate of $\mathcal{T}_{p\,j}^{\mathrm{eff}} \geqslant 3$ does not peak near the ramp regions of the 52 IP shocks examined herein is consistent with the apparent lack of dependence on $\mathcal{T}_{i\,\mathrm{tot}}^{e}$ found in previous work (e.g., Rodriguez & Gurnett 1975; Wilson et al. 2007). Note that these rates are significantly higher than those estimated for the ambient solar wind in a recent study (e.g., Wilson et al. 2018).

The critical drift speed between electrons and ions for a current-driven IAW can be analytically derived for two isotropic Maxwellians that generate a current. The critical drift is known to depend upon $\mathcal{T}_{i\,\mathrm{tot}}^{e}$ (e.g., Gurnett & Bhattacharjee 2005). This critical drift threshold for current-driven IAWs, ignoring the details of the ion and electron populations, is satisfied for ∼4.78% of the 12,081 VDFs for *Criteria AT* that had solutions for both electron and proton data. However, as discussed in Priest & Sanderson (1972), the presence of gradients in the temperature and density reduce this idealized critical drift by factors of ∼2–8. This increases the number of VDFs satisfying the critical drift threshold to ∼5.2%–10.4%. These rates require context to appreciate their magnitudes.

To provide context, some statistical calculations will be performed based upon the observations and relying upon the near ubiquity of IAWs in and around collisionless shock waves (e.g., Gurnett et al. 1979b; Fuselier & Gurnett 1984; Wilson et al. 2007; Breneman et al. 2013; Chen et al. 2018; Goodrich et al. 2018). The typical collisionless shock ramp thickness is anywhere from $\gtrsim 1\langle\lambda_e\rangle_{\mathrm{up}}$ to $\lesssim 43\langle\lambda_e\rangle_{\mathrm{up}} \sim 1\langle\lambda_i\rangle_{\mathrm{up}}$ (e.g., Hobara et al. 2010; Mazelle et al. 2010). For the 52 IP shocks examined herein, the following are satisfied for 90% of the events:

1. $1.2\,\mathrm{km} \lesssim \langle\lambda_e\rangle_{\mathrm{up}} \lesssim 4.2\,\mathrm{km}$;
2. $155\,\mathrm{km\,s^{-1}} \lesssim \langle|V_{\mathrm{shn}}|\rangle_{\mathrm{up}} \lesssim 700\,\mathrm{km\,s^{-1}}$; and
3. $1\,\mathrm{km} \lesssim L_{\mathrm{sh}} \lesssim 180\,\mathrm{km}$.

These shock-ramp thicknesses correspond to timescales of ∼0.002–1.2 s in the spacecraft frame, or $\sim 10^{-5}$–0.008% of the total time window examined for each IP shock. The duration of each electron VDF is ∼3 s,[19] which means the shock ramps are at most ∼30% of the minimum cadence of the Wind 3DP instrument. Thus any given VDF cannot parameterize only the shock ramp, and the instruments cannot directly measure the shock-ramp currents.

Despite the limitation of the particle data time resolution and unrealistic VDF profile assumptions in the theory, there were still nearly 600 VDFs that satisfied the critical drift threshold for current-driven IAWs. This corresponds to roughly 11 VDFs for each of the 52 IP shocks examined herein or a total duration more than 27 times that of the longest shock ramp in this study. Further, there were nearly 3500 VDFs (or ∼67 per IP shock) that satisfy $\mathcal{T}_{p\,j}^{\mathrm{eff}} \geqslant 3$ (i.e., the often-quoted temperature ratio threshold for IAWs). The IAWs of interest here should affect the electron VDFs on timescales much shorter than the integration time; thus the Wind 3DP instrument should only observe the post-instability form.

The *Criteria DN* VDFs have larger core self-similar exponents (s_{ec}, p_{ec}, and q_{ec}) than *Criteria UP* VDFs, with the strongest shocks consistently showing flattops (i.e., $p_{ec} \geqslant 4$) for minutes to hours in the downstream, similar to terrestrial bow shock observations. The larger core exponents in the downstream regions combined with IAW amplitudes positively correlated with Mach number (e.g., Wilson et al. 2007) is consistent with IAWs stochastically accelerating the core electrons (e.g., Dum et al. 1974; Dum 1975). This type of stochastic acceleration is qualitatively referred to as inelastic scattering throughout this three-part study. However, such a change in VDF profile has also been interpreted as due to the acceleration by quasi-static cross-shock electric fields (e.g., Scudder et al. 1986; Schwartz et al. 1988, 2011; Hull et al. 2001; Mitchell & Schwartz 2014; Schwartz 2014). Note that for both s_{ec} and p_{ec}, the differences between *Criteria LM* and *Criteria HM* shocks are not statistically significant. That is, theory and observation suggest that the magnitude of both the quasi-static cross-shock electric fields and IAW amplitudes should increase with increasing Mach number. Therefore, if IAWs are affecting the core electrons, are they increasing the exponent or the temperature or both? If so, why and how? Similar questions arise regarding the quasi-static cross-shock electric field explanation. Kinetic simulations are required to resolve this discrepancy and are beyond the scope of this study.

Finally, two more instabilities will be discussed that also affect the ions since most previous instability work has focused on the ions (e.g., Maruca et al. 2012; Kasper et al. 2013; Klein et al. 2017, 2018). The purpose is to examine the differences in the particle populations near IP shocks versus what is typically considered ambient solar wind. The threshold for both the mirror and firehose instabilities can also be calculated following the approach[20] in Chen et al. (2016). Using only

[19] The instrument is actually triggered on the Sun pulse from the Sun sensor, which depends on the spin rate of the spacecraft bus. The spin period for Wind has remained near ∼3 s for the entirety of the mission but varies by a ∼0.1 s, depending on date and time.

[20] Note that the major differences between Chen et al. (2016) and this work are that this work does not include secondary proton beams; here we separate the electron components rather than treating them all as one population, and we include IP shocks.

Table 1
Fit Parameters for Figure 7

Y	$A \times 10^{-3}$[a]	B[b]	C[c]	$\tilde{\chi}^2$[d]	$\Sigma_{\rm fit}$[e]
$T_{\rm eff,\parallel}$	0.4 ± 0.3[f]	2.13 ± 0.11	0.89 ± 0.27	1.7	4.5
$T_{\rm eff,\perp}$	0.3 ± 0.4	1.67 ± 0.27	0.74 ± 0.39	1.1	2.7
$T_{\rm eff,tot}$	5.0 ± 4.0	1.59 ± 0.11	0.41 ± 0.31	1.4	3.3
$T_{ec,\parallel}$	0.5 ± 0.5	2.11 ± 0.10	0.87 ± 0.28	1.8	4.7
$T_{ec,\perp}$	3.0 ± 3.0	1.71 ± 0.22	0.78 ± 0.37	1.3	3.0
$T_{ec,\rm tot}$	1.0 ± 1.0	1.96 ± 0.20	0.89 ± 0.34	1.3	3.1
$T_{i,\parallel}$	2.0 ± 3.0	1.77 ± 0.23	1.44 ± 0.41	3.8	9.1
$T_{i,\perp}$	8.0 ± 8.0	1.61 ± 0.16	2.22 ± 0.60	2.1	5.5
$T_{i,\rm tot}$	3.0 ± 4.0	1.76 ± 0.18	2.10 ± 0.52	2.5	6.4

Notes. For symbol definitions, see Appendix A.
[a] Constant multiplier in power law.
[b] Exponent in power law.
[c] Constant offset in power law.
[d] Reduced chi-squared of fit.
[e] Standard error between fit and data.
[f] Values shown are larger by a factor of 10^{+3}.

VDF solutions when all five particle populations have finite velocity moments, the plasma is unstable to the firehose instability ∼1.3% of the time and mirror ∼13.5%. These rates are ∼10 and ∼20 times larger, respectively, than the rates found by Chen et al. (2016). It may not be surprising to find that VDFs are statistically more unstable near IP shocks than the ambient solar wind, since the shock itself is a constant source of multiple types of free energy. However, these rates do not significantly change if the time range of analysis is limited to ±20 minutes of the shock ramp center, suggesting the enhanced rates are either due to the separation of electron components or the lack of inclusion of a secondary proton beam. Despite this, the *Criteria UP* VDFs should be treated as generally being more unstable than time periods that intentionally avoid IP shocks.

As a final note, the instability analysis presented in this section should be interpreted with care. The rates calculated are based upon thresholds and do not directly imply anything about whether an observable wave amplitude would result. For instance, the threshold for the whistler instabilities are for growth rates at 10% of the proton cyclotron frequency (i.e., >18,000 times longer than a single electron cyclotron period). Therefore, that only ∼3% of the VDFs are stable does not imply large amplitude whistler waves should be observed for nearly all intervals examined herein.[21] That is, in the cases where the instability thresholds are barely surpassed, the resulting fluctuation amplitudes may be so small that they are below the noise floor of many instruments. Further, the separation of the electron VDF into three populations, all non-Maxwellian, is different than the two drifting bi-Maxwellians assumed by Gary et al. (1994). Thus, the large fraction of VDFs satisfying instability thresholds presented herein should not be interpreted as most time intervals exhibiting large amplitude electromagnetic fluctuations.

[21] However, such high rates are consistent with previous studies finding whistler waves to be common downstream of IP shocks (e.g., Coroniti et al. 1982; Lengyel-Frey et al. 1994, 1996) and in the ambient solar wind (e.g., Lengyel-Frey et al. 1996; Neubauer & Musmann 1977).

5. Energy Partition

5.1. Temperature Differences

In this section, the changes in the fit results across all shocks are examined. The data are presented as the median of all permutations of the difference, $\widetilde{\Delta Q}$, of parameter Q between the upstream and downstream values for each IP shock. The uncertainties for the fit parameters are half the magnitude of the difference between $X_{5\%}$ and $X_{95\%}$. The uncertainties for the macroscopic shock parameters result from the standard propagation of uncertainties given by the values in the Wind shock database.

These medians with uncertainties were then fit to a model power-law function, $Y = A\,X^B + C$, assuming Poisson weights, where X is one of the macroscopic shock parameters and Y is one of the medians of all permutations of the difference (or ratio) across the shock. Given that the shock must transform the change in bulk kinetic energy, the obvious shock parameter to examine is the change in kinetic energy, $\Delta\overline{KE}_{\rm shn}$ (see Appendix A), across the shock.[22]

Figure 7 shows the relationship between the change in temperature versus the change in shock kinetic energy, and Table 1 shows the values of the fit parameters with goodness of fit estimates. Here, the $\widetilde{\Delta T_{s,j}}$ values represent the median[23] of all the permuted temperature differences between downstream and upstream for each IP shock. The $\Delta\overline{KE}_{\rm shn}$ values are just computed from the $\langle|U_{\rm shn}|\rangle_j$ values from the Wind shock database. The uncertainties are calculated using the standard propagation of uncertainties.

The first thing to notice is that the relationship is not linear. In fact, several previous studies examined the change in temperature and found positive correlations between $\Delta\bar{T}_{e,\rm tot}$ and variants of $\Delta\overline{KE}_{\rm shn}$ (e.g., Thomsen et al. 1987, 1993; Schwartz et al. 1988; Hull et al. 2000). However, if one examines the plots of $\widetilde{\Delta T}_{e,\rm tot}$ versus $\Delta\overline{KE}_{\rm shn}$ in each of these studies, it is not clear whether the trend is linear or otherwise. For instance, examination of Figures 5 and 6 in Feldman et al. (1983c) do not appear to have a linear trend. The linear relationship between $\Delta\bar{T}_{e,\rm tot}$ and $\Delta\overline{KE}_{\rm shn}$ found by Hull et al. (2000) required that they ignore shocks with $\Delta\overline{KE}_{\rm shn} < 100$ eV in the fit. The relationship between $\Delta\bar{T}_{e,\rm tot}$ and $\Delta\bar{U}^2_{\rm shn}$ found by Fitzenreiter et al. (2003), however, did appear to be linear. Note that many of the previous studies examined the higher Mach number terrestrial bow shock.

However, it is not unreasonable to assume that a linear relationship would exist if the energy conversion was linear. That is, if the irreversible transformation of excess kinetic energy across the shock[24] into particle heating occurred directly with no intermediary processes,[25] one may expect that a linear relationship would exist with the change in electron and ion temperature with some associated efficiency. A linear

[22] All other relevant shock parameters were examined and weaker relationships were found between $\langle M_f\rangle_{\rm up}$ (not shown) and the permuted differences of $\beta_{eb,j}$ and $P_{ec,j}$. Weak relationships were also observed between $\Delta\bar{U}_{\rm shn}$ (not shown) and the permuted differences of the following: $\mathcal{A}_{ec}$, $\mathcal{A}_{\rm eff}$, $T_{ec,j}$, $T_{{\rm eff},j}$, $T_{p,j}$, and $T_{i,j}$.
[23] Note that the use of the average of all permutations of the differences did not yield significantly different results than the median.
[24] Some of the total energy transformation must be irreversible to initiate a shock from a nonlinearly steepening wave, but once initiated, reversible processes can maintain the shock (e.g., Shu 1992).
[25] For instance, $\Delta\overline{KE}_{\rm shn} \rightarrow \Delta\bar{T}_{e,\rm tot}$.

relationship also requires, in general, fewer assumptions to model. That is, the scatter plot of points in previous studies could have just as easily been fit to a nonlinear function like a power law, though it is likely these authors chose a linear relationship, as that is the simplest possibility.

One should also note that the exponents for $\widetilde{\Delta T}_{ec,\parallel}$ and $\widetilde{\Delta T}_{\mathrm{eff},\parallel}$ are larger than all exponents of $\widetilde{\Delta T}_{i,j}$. However, if the five magenta points at large $\Delta\overline{KE}_{\mathrm{shn}}$ are included in the fits, the exponents for $\widetilde{\Delta T}_{ec,j}$ and $\widetilde{\Delta T}_{\mathrm{eff},j}$ would decrease more than $\widetilde{\Delta T}_{i,j}$. Note that previous work has either inferred (e.g., Ghavamian et al. 2007, 2014) or showed with in situ measurements that stronger shocks heat ions more than electrons (e.g., Schwartz et al. 1988; Thomsen et al. 1993; Masters et al. 2011). In fact, Schwartz et al. (1988) and others have even noticed that $\Delta\bar{T}_{e,\mathrm{tot}}/\Delta\bar{T}_{t,\mathrm{tot}} \propto \langle M_A\rangle_{\mathrm{up}}^{-1}$. Therefore, the change in slope/trend at larger $\Delta\overline{KE}_{\mathrm{shn}}$ may be indicative of differences in shock energy dissipation at stronger shocks, as suggested by trends in previous work.

Even when the five magenta points at large $\Delta\overline{KE}_{\mathrm{shn}}$ (i.e., magenta points in upper right-hand corner of each panel of Figure 7) were included in the fit, the linear fit had much larger $\tilde{\chi}^2$ or Σ_{fit} values (not shown). Though it is also fair to argue that the fits shown in Figure 7 are not really good fits despite the low $\tilde{\chi}^2$ or Σ_{fit} values shown in Table 1. That is, the data have large uncertainties and large relative spread for each $\Delta\overline{KE}_{\mathrm{shn}}$, as evidenced by the green lines on either side of the red fit lines. Therefore, it is likely that if even stronger shocks were added to this data set, the power-law trend presented in Figure 7 would need to be modified by either an exponential roll-over or higher-order terms or the trend would entirely fall apart. Thus, these fits should be treated with caution and/or skepticism.

To verify that the use of the median on the permutations of all differences was not causing the nonlinearity, the same temperature differences were plotted versus $\Delta\overline{KE}_{\mathrm{shn}}$ but now using $\Delta\bar{T}_{s,j}$ instead of $\widetilde{\Delta T}_{s,j}$ (not shown). That is, the average over each region was calculated as a single scalar prior to finding the difference between the regions. The nonlinear fit lines were still a better match to the results than a linear line. Thus, the nonlinear relationship between the temperature increase and the change in kinetic energy across the shock appears to be real at least for low $\Delta\overline{KE}_{\mathrm{shn}}$.

Most of the earlier work looking at the dependence of $\Delta\bar{T}_{s,j}$ on $\Delta\overline{KE}_{\mathrm{shn}}$ focused on the Earth's bow shock, which is typically higher Mach number (i.e., $\langle M_f\rangle_{\mathrm{up}} \gtrsim 3$–$10$) than those examined herein. The Mach numbers in this study satisfy $1.01 \leqslant \langle M_f\rangle_{\mathrm{up}} \leqslant 6.4$, with 90% satisfying ∼1.15–4.00, and a median of ∼1.86. Note that 45 of the 52 IP shocks examined herein satisfied $\langle M_f\rangle_{\mathrm{up}} < 3$. Further, the relationship between $\langle M_f\rangle_{\mathrm{up}}$ and $\Delta\overline{KE}_{\mathrm{shn}}$ is not linear. This begs the question of what could cause the energy transformation from $\Delta\overline{KE}_{\mathrm{shn}}$ into $\Delta\bar{T}_{s,j}$ to be nonlinear, if the trend is real.

Regardless, the fraction of $\Delta\overline{KE}_{\mathrm{shn}}$ distributed to each of the populations shown in Figure 7, for 90% of events (i.e., $X_{5\%}$ to $X_{95\%}$ range), satisfy the following:

1. $1.5\% \lesssim \widetilde{\Delta T}_{ec,j}\big/\Delta\overline{KE}_{\mathrm{shn}} \lesssim 34\%$;
2. $0.8\% \lesssim \widetilde{\Delta T}_{\mathrm{eff},j}\big/\Delta\overline{KE}_{\mathrm{shn}} \lesssim 41\%$; and
3. $1.4\% \lesssim \widetilde{\Delta T}_{i,j}\big/\Delta\overline{KE}_{\mathrm{shn}} \lesssim 63\%$.

Although these ratios are mostly uniform for all j for both electron populations, the $\widetilde{\Delta T}_{i,\parallel}\big/\Delta\overline{KE}_{\mathrm{shn}}$ range is systematically smaller than the other two components. That is, if one separates the perpendicular and total from the parallel components then 90% of the events would satisfy

1. $5.8\% \lesssim \widetilde{\Delta T}_{i,\{\perp,tot\}}\big/\Delta\overline{KE}_{\mathrm{shn}} \lesssim 63\%$; and
2. $1.4\% \lesssim \widetilde{\Delta T}_{i,\parallel}\big/\Delta\overline{KE}_{\mathrm{shn}} \lesssim 40\%$.

Similarly the median values for $\widetilde{\Delta T}_{ec,j}\big/\Delta\overline{KE}_{\mathrm{shn}}$ and $\widetilde{\Delta T}_{\mathrm{eff},j}\big/\Delta\overline{KE}_{\mathrm{shn}}$ are in the ∼7.6%–9.3% range while the $\widetilde{\Delta T}_{i,j}\big/\Delta\overline{KE}_{\mathrm{shn}}$ median values satisfy ∼10.7%–17.9%, with the parallel component being the smallest. In summary, the electron core and effective populations only gain ∼40%–80% of what the ions do in thermal energy across the shock for these events.

5.2. Energy Density Differences

In this section, the partition of energy among the five primary constituent particle populations will be discussed. These five are the electron core ($s = ec$), halo ($s = eh$), beam/strahl ($s = eb$), and ion proton ($s = p$) and alpha-particle ($s = \alpha$) populations. Similar to Section 5.1, the median of all permutations of the differences will be discussed.

The normalized pressures, $\widetilde{\Delta\Pi}_{s,j}$ and $\widetilde{\Delta\psi}_{s,j}$, were plotted (not shown) versus θ_{Bn}, $\langle|V_{\mathrm{shn}}|\rangle_{\mathrm{up}}$, $\langle|U_{\mathrm{shn}}|\rangle_{\mathrm{up}}$, $\langle M_f\rangle_{\mathrm{up}}$, $\langle M_A\rangle_{\mathrm{up}}$, $\langle M_{Te}\rangle_{\mathrm{up}}$, $\Delta\bar{U}_{\mathrm{shn}}$, $\Delta\overline{KE}_{\mathrm{shn}}$, and $\Delta\bar{\xi}_{\mathrm{shn}}$ (i.e., every macroscopic shock parameter predicted to be of importance here). In the following, weak correlations imply there is a trend, but the large scatter and multiple outliers make interpretation difficult. Moderate correlations are for clear trends but still with a significant spread in data (e.g., similar to $\widetilde{\Delta T}_{s,j}$ plots in Figure 7). There were no good correlations observed for any pair of parameters examined—only a few moderate correlations and several weak correlations (not shown).

For reference, the following will show parameters as $X_{5\%} \lesssim X \lesssim X_{95\%}$, $\tilde{X}$, for the 52 IP shocks examined herein:

1. $4.07\% \lesssim \widetilde{\Delta\Pi}_{ec,\,j} \lesssim 41.0\%$, ∼12.7%;
2. $1.15\% \lesssim \widetilde{\Delta\Pi}_{eh,j} \lesssim 10.6\%$, ∼3.85%;
3. $0.30\% \lesssim \widetilde{\Delta\Pi}_{eb,j} \lesssim 7.46\%$, ∼3.22%;
4. $4.36\% \lesssim \widetilde{\Delta\Pi}_{\mathrm{eff},j} \lesssim 36.1\%$, ∼12.8%;
5. $4.05\% \lesssim \widetilde{\Delta\Pi}_{p,j} \lesssim 36.1\%$, ∼12.5%; and
6. $0.15\% \lesssim \widetilde{\Delta\Pi}_{\alpha,j} \lesssim 9.05\%$, ∼2.33%.

If the analysis is limited to *Criteria LM* shocks, then these relations go to

1. $2.36\% \lesssim \widetilde{\Delta\Pi}_{ec,j} \lesssim 38.3\%$, ∼12.8%;
2. $1.06\% \lesssim \widetilde{\Delta\Pi}_{eh,j} \lesssim 9.49\%$, ∼3.57%;
3. $0.74\% \lesssim \widetilde{\Delta\Pi}_{eb,j} \lesssim 6.87\%$, ∼2.43%;
4. $4.36\% \lesssim \widetilde{\Delta\Pi}_{\mathrm{eff},j} \lesssim 35.3\%$, ∼12.4%;
5. $4.36\% \lesssim \widetilde{\Delta\Pi}_{p,j} \lesssim 35.3\%$, ∼12.4%; and
6. $0.15\% \lesssim \widetilde{\Delta\Pi}_{\alpha,j} \lesssim 9.05\%$, ∼2.35%.

Finally, if the analysis is limited to *Criteria HM* shocks, then these relations go to

1. $4.51\% \lesssim \widetilde{\Delta\Pi}_{ec,j} \lesssim 43.8\%$, ∼10.3%;

2. $1.83\% \lesssim \widetilde{\Delta\Pi}_{eh,j} \lesssim 11.6\%$, $\sim 6.21\%$;
3. $0.97\% \lesssim \widetilde{\Delta\Pi}_{eb,j} \lesssim 7.46\%$, $\sim 5.96\%$;
4. $4.40\% \lesssim \widetilde{\Delta\Pi}_{\mathrm{eff},j} \lesssim 40.4\%$, $\sim 13.4\%$;
5. $3.73\% \lesssim \widetilde{\Delta\Pi}_{p,j} \lesssim 40.4\%$, $\sim 13.7\%$; and
6. $0.43\% \lesssim \widetilde{\Delta\Pi}_{\alpha,j} \lesssim 3.48\%$, $\sim 1.68\%$.

Note that the Wind SWE Faraday cups have difficulty separating alpha particles from protons and finding good nonlinear fit solutions in the immediate downstream of the stronger shocks in this study, which is likely affecting the upper bounds of both $\widetilde{\Delta\Pi}_{p,j}$ and $\widetilde{\Delta\Pi}_{\alpha,j}$. The reason for emphasizing this point is that previous work (e.g., Schwartz et al. 1988; Thomsen et al. 1993; Masters et al. 2011) found more energy going to the ions as the Mach number increases but the core electrons seem comparable to the protons here. A possible difference may be that previous work examined the total ion and electron VDFs, which may blur the differences in trends between the various components of each species. It is also worth noting that the $\widetilde{\Delta\Pi}_{s,j}$ values result from the absolute value of the differences (i.e., the actual change may be negative for one population).

To determine which population gained more thermal energy density across the shocks, the ratio of the electron component to proton thermal energy densities are examined where the parameters are shown as $X_{5\%} \lesssim X \lesssim X_{95\%}$, $\tilde{X}$. The values the 52 IP shocks examined herein are as follows:

1. $16.9\% \lesssim \widetilde{\Delta P}_{ec,j}/\widetilde{\Delta P}_{p,j} \lesssim 391\%$, $\sim 101\%$;
2. $1.11\% \lesssim \widetilde{\Delta P}_{eh,j}/\widetilde{\Delta P}_{p,j} \lesssim 41.3\%$, $\sim 5.41\%$;
3. $0.47\% \lesssim \widetilde{\Delta P}_{eb,j}/\widetilde{\Delta P}_{p,j} \lesssim 18.3\%$, $\sim 2.55\%$; and
4. $19.6\% \lesssim \widetilde{\Delta P}_{\mathrm{eff},j}/\widetilde{\Delta P}_{p,j} \lesssim 453\%$, $\sim 107\%$.

If the analysis is limited to *Criteria LM* shocks, then these relations go to

1. $15.8\% \lesssim \widetilde{\Delta P}_{ec,j}/\widetilde{\Delta P}_{p,j} \lesssim 391\%$, $\sim 89.7\%$;
2. $0.94\% \lesssim \widetilde{\Delta P}_{eh,j}/\widetilde{\Delta P}_{p,j} \lesssim 28.8\%$, $\sim 5.41\%$;
3. $0.47\% \lesssim \widetilde{\Delta P}_{eb,j}/\widetilde{\Delta P}_{p,j} \lesssim 22.2\%$, $\sim 2.37\%$; and
4. $17.3\% \lesssim \widetilde{\Delta P}_{\mathrm{eff},j}/\widetilde{\Delta P}_{p,j} \lesssim 453\%$, $\sim 102\%$.

Finally, if the analysis is limited to *Criteria HM* shocks, then these relations go to

1. $36.4\% \lesssim \widetilde{\Delta P}_{ec,j}/\widetilde{\Delta P}_{p,j} \lesssim 372\%$, $\sim 182\%$;
2. $2.82\% \lesssim \widetilde{\Delta P}_{eh,j}/\widetilde{\Delta P}_{p,j} \lesssim 49.3\%$, $\sim 8.76\%$;
3. $0.54\% \lesssim \widetilde{\Delta P}_{eb,j}/\widetilde{\Delta P}_{p,j} \lesssim 10.0\%$, $\sim 3.42\%$; and
4. $22.0\% \lesssim \widetilde{\Delta P}_{\mathrm{eff},j}/\widetilde{\Delta P}_{p,j} \lesssim 391\%$, $\sim 199\%$.

Therefore, the change in core electron thermal pressure is comparable to or larger than that for the protons, even for the *Criteria HM* shocks, unexpectedly. For the *Criteria LM* shocks, the core electrons receive roughly the same heating as the protons, consistent with previous results (e.g., Schwartz et al. 1988). Note that despite the use of pressure here as a measure of thermal energy density, none of these processes are occurring in a thermodynamic system. That is, there is no well-defined equation of state for each of the particle populations.

In summary, none of the energy density ratios showed a clear dependence upon any macroscopic shock parameter. None of the $\widetilde{\Delta\Pi}_{s,j}$ or $\widetilde{\Delta\psi}_{s,j}$ cared about θ_{Bn}—that is, the change in the ratio of thermal energy density to both the total pressure and total energy density is independent of shock geometry. In other words, the shock geometry does not appear to affect the change in the partition of energy among the five major particle populations. The most correlations were found with $\Delta\bar{U}_{\mathrm{shn}}$, but again none of them were good. The only good correlation was observed between $\Delta\bar{\xi}_{\mathrm{shn}}$ and $\widetilde{\Delta\epsilon_j}$ (not shown; i.e., the change in total energy density increases with increasing change in shock kinetic energy density). This merely shows that as the available free energy increases, the total internal energy increases, as expected.

Finally, the absolute changes in normalized partial pressures were dominated by the core electrons and protons with the suprathermal electrons and alpha-particles serving as minor constituents, which is again expected. However, the absolute differences discussed in this section do not inform us whether the change is positive or negative. Further, somewhat unexpectedly, the core electron pressure changes were often larger than those for the protons for *Criteria HM* shocks, while for *Criteria LM* shocks, the changes were closer to previous observations (e.g., Schwartz et al. 1988). Again, some of this is most likely due to the issues facing the Wind SWE Faraday cups downstream of the strongest shocks in this study. However, the larger-than-unity ratios of $\widetilde{\Delta P}_{ec,j}/\widetilde{\Delta P}_{p,j}$ for even *Criteria LM* shocks were not really expected. To help address this, SEA plots are shown to illustrate the trends in $\Delta\Pi_{s,j}$ versus time in the following section.

5.3. Thermal Energy Density Trends

In this section, the partition of energy among the five primary constituent particle populations will be discussed. These five are the electron core ($s = ec$), halo ($s = eh$), beam/strahl ($s = eb$), and ion proton ($s = p$) and alpha-particle ($s = \alpha$) populations. Similar to Section 3, SEA plots will be presented.

Since none of the $\widetilde{\Delta Q}$ seemed to show very good correlations with any macroscopic shock parameter predicted to be of importance, the statistical trend of the normalized energy densities directly using SEA were examined. The purpose is to see if any clear trend versus time(space) emerges that is not reflected in macroscopic differences or ratios. Note that the SEA plots involve the calculation of one-variable statistics for all points within a given time bin, while the $\widetilde{\Delta Q}$ values are calculated on a shock-by-shock basis.

Figure 8 shows the running median only from SEA of the partial thermal pressures, $\Pi_{s,j}$, of each of the major particle populations in the solar wind, including the core electrons (blue lines), halo electrons (red lines), beam/strahl electrons (orange lines), protons (magenta lines), and alpha-particles (purple/violet lines). First, $\Pi_{ec,j}$ and $\Pi_{p,j}$ dominate at all times for all selection criteria, as expected. Second, the general trend of all electron populations is for their fractional thermal energy density to reduce across the shock ramp except for $\Pi_{ec,j}$ for *Criteria HM* shocks. Both the $\Pi_{eh,j}$ and $\Pi_{eb,j}$ electrons consistently decrease across the shock, with the weakest change across *Criteria PA* shocks. The $\Pi_{eb,j}$ show a continual decreasing trend across *Criteria HM* shocks with a distinct jump at the shock ramp in contrast to $\Pi_{eh,j}$, which basically levels off and recovers downstream. There are also several intervals where $\Pi_{ec,j}$ and $\Pi_{p,j}$ seem to oscillate exactly out of phase from each other, likely owing to pressure balance

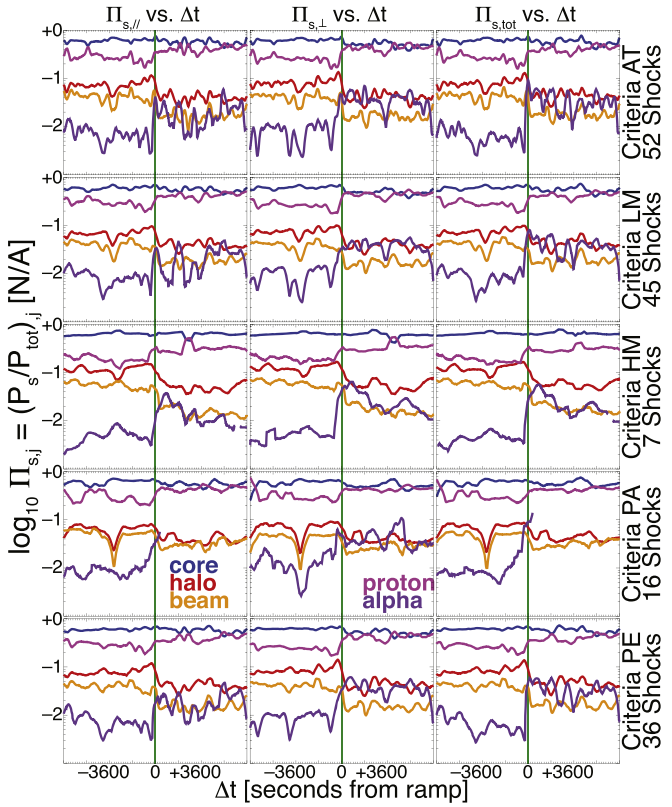


Figure 8. Running median (e.g., red lines in Figure 1) from the SEA of the partial thermal pressures, $\Pi_{s,j}$ (see Appendix A for parameter definitions), for each of the following particle populations: core electrons (blue lines), halo electrons (red lines), beam/strahl electrons (orange lines), protons (magenta lines), and alpha-particles (purple/violet lines). Unlike previous SEA plots, these are not normalized to an upstream median value. The vertical green line indicates the ramp center time. All panels have uniform horizontal and vertical axis ranges.

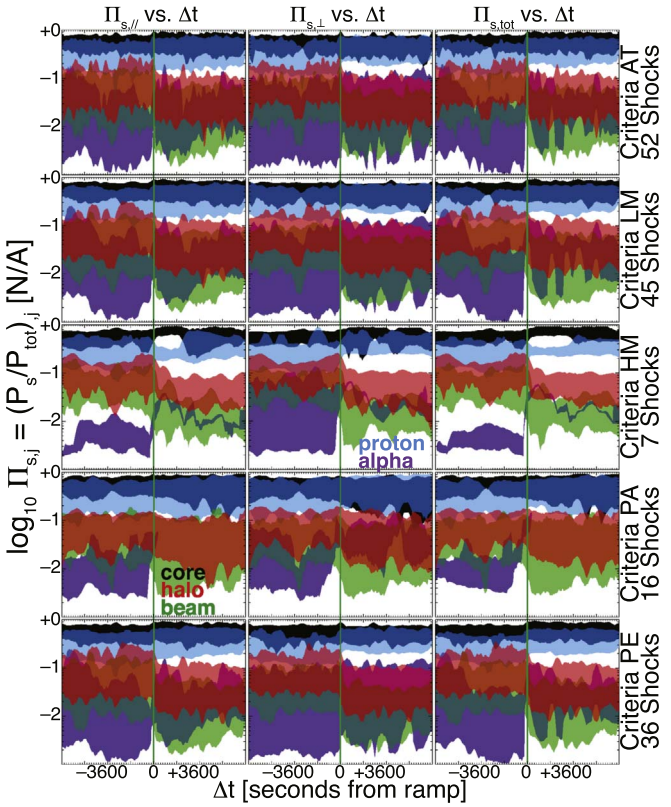


Figure 9. Shaded regions bounded by $X_{5\%}$ and $X_{95\%}$ (e.g., cyan lines in Figure 1) from the SEA of the partial thermal pressures, $\Pi_{s,j}$ (see Appendix A for parameter definitions), for each of the following particle populations: core electrons (black regions), halo electrons (red regions), beam/strahl electrons (green regions), protons (cyan regions), and alpha-particles (purple/violet regions). Again, unlike previous SEA plots, these are not normalized to an upstream median value. The vertical green line indicates the ramp center time. All panels have uniform horizontal and vertical axis ranges.

features near these shocks. The interesting aspect is that they are common/strong enough to show up in a running median constructed from SEA on 52 different shocks.

In general, the following are satisfied for ∼90% of all data for *Criteria AT* (i.e., between $X_{5\%}$ and $X_{95\%}$), from largest to smallest (see Table B2):

1. $25\% \lesssim \Pi_{ec,j} \lesssim 92\%$;
2. $13\% \lesssim \Pi_{p,j} \lesssim 72\%$;
3. $1\% \lesssim \Pi_{eh,j} \lesssim 18\%$;
4. $0.3\% \lesssim \Pi_{eb,j} \lesssim 11\%$; and
5. $0.2\% \lesssim \Pi_{\alpha,j} \lesssim 11\%$.

These are the partitions of thermal energy density for all time periods. When the data are separated into upstream and downstream, things change slightly but not tremendously. For *Criteria UP*, sorted from largest to smallest, the following are satisfied:

1. $27\% \lesssim \Pi_{ec,j} \lesssim 85\%$;
2. $11\% \lesssim \Pi_{p,j} \lesssim 68\%$;
3. $1\% \lesssim \Pi_{eh,j} \lesssim 23\%$;
4. $0.7\% \lesssim \Pi_{eb,j} \lesssim 15\%$; and
5. $0.1\% \lesssim \Pi_{\alpha,j} \lesssim 9\%$.

For *Criteria DN* , sorted from largest to smallest, the following are satisfied:

1. $24\% \lesssim \Pi_{ec,j} \lesssim 95\%$;
2. $15\% \lesssim \Pi_{p,j} \lesssim 74\%$;
3. $1\% \lesssim \Pi_{eh,j} \lesssim 15\%$;
4. $0.2\% \lesssim \Pi_{eb,j} \lesssim 8\%$; and
5. $0.2\% \lesssim \Pi_{\alpha,j} \lesssim 13\%$.

To illustrate that the energy partitions shown as running medians in Figure 8 can be characteristic of most of the data, Figure 9 shows the same parameters for the same populations but as shaded regions bounded by $X_{5\%}$ and $X_{95\%}$. What is immediately clear is that again $\Pi_{ec,j}$ and $\Pi_{p,j}$ dominate at all times, except for some transient excursions to large values for $\Pi_{eh,j}$. Both $\Pi_{eb,j}$ and $\Pi_{\alpha,j}$ have relatively large spreads in the range between percentiles, but they still follow the same trends illustrated by the running median. That is, the suprathermal electron fractional thermal energy density decreases while both ion species increase. The abrupt end in $\Pi_{\alpha,j}$ data for *Criteria PA* shocks in both Figures 8 and 9 are due to low statistics owing to difficulties in finding high quality fits for the alpha-particle peak (e.g., see the SWE fit flag requirements in Wilson et al. 2018).

It is also clear that *Criteria HM* shocks have the largest separation between $\Pi_{ec,j}$ and $\Pi_{p,j}$ for all time periods compared to other selection criteria. The downstream running median values for *Criteria LM* and *Criteria PE* shocks oscillate out of phase, but this is not directly reflected in

$X_{5\%}$–$X_{95\%}$. *Criteria PA* shocks exhibit the most overlap in $X_{5\%}$–$X_{95\%}$, and *Criteria HM* shocks have the least. In both the running $\tilde{X}$ and $X_{5\%}$–$X_{95\%}$, $\Pi_{eh,j}$ shows a very clear decrease across the shock except for *Criteria PA* shocks where the change in $X_{5\%}$ and $X_{95\%}$ is more difficult to observe. The abrupt drop in $\Pi_{eh,j}$ and $\Pi_{eb,j}$ across shocks is likely related to the drop in $n_{eh}/n_{\rm eff}$ and $n_{eb}/n_{\rm eff}$ across the shocks because the associated temperatures show slight increases across the shock (see additional SEA plots of $T_{s,j}$ found in Wilson et al. 2020).

6. Discussion

Superposed epoch analysis (SEA) of the fit results show that the general trend of the normalized (to the upstream median) exponents for all electron components increases across the shock ramp for all selection criteria.[26] That is, the suprathermal electron tails are steeper and the core electrons at low velocities are flatter, relative to a Maxwellian, and steeper at higher energies. The normalized density, $n_s/n_{\rm eff}$, SEA plots show a general increase (relative to the upstream median) across the shock ramp for the core, but decrease for both halo and beam/strahl, for all selection criteria. That is, only the fraction of core electrons increases across the shock. Finally, the ratio of the partial-to-total pressure, $\Pi_{s,j}$, for the protons and alpha particles increase across the shock, while the ratio for all electron populations decrease.

An illustrative example of the possible electron VDF evolution for the weakest and strongest shocks is qualitatively shown in Figure 10. The electron VDF starts as a narrow peaked distribution with hard tails and evolves into an almost box-like distribution with weaker, soft tails. Thus, the energy density becomes consolidated into the core population. It is clear that stronger shocks have a different downstream profile than weaker shocks. The strong shock example is indicative of the strongest shocks in this study and similar to observations downstream of the terrestrial bow shock. The larger exponents, in all three electron components, for the strong shock example produces a flatter peak in the core and steeper slopes in the halo and beam/strahl. Although the number density of the downstream weak shock example is lower than for the strong shock example, the phase space density peak is almost an order of magnitude larger due to the smaller exponents and thermal speeds. Potential reasons for the change in profile are discussed later.

The majority of the thermal energy density is held in the core electrons with $\Pi_{ec,j} \sim 25\%$–92% (i.e., fraction of the total pressure) and the protons taking up most of the rest with $\Pi_{p,j} \sim 13\%$–72% for *Criteria AT*. For $\sim$95% of the suprathermal electron and alpha-particle velocity moments, none individually satisfy $\Pi_{s,j} > 18\%$. That is, the partition of thermal energy density is completely dominated by the core electrons and protons while the suprathermal electrons and alpha-particles serve as mostly minor contributors. Further, the magnitude of the change in partial pressures, $\widetilde{\Delta\Pi}_{s,j}$, across the 52 IP shocks examined herein (shown as $X_{\rm min} \lesssim X \lesssim X_{\rm max}$) satisfies the following:

1. $1.7\% \lesssim \widetilde{\Delta\Pi}_{ec,j} \lesssim 55.8\%$;
2. $0.6\% \lesssim \widetilde{\Delta\Pi}_{eh,j} \lesssim 35.9\%$;

[26] Except for *Criteria UP* and *Criteria DN* , of course.

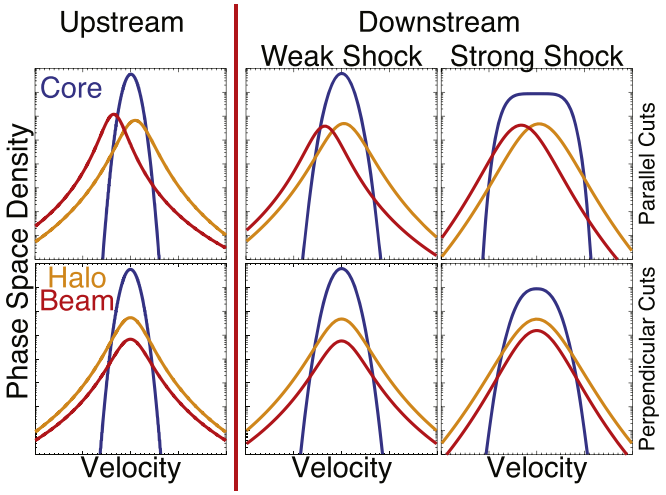


Figure 10. Cartoon example of the evolution of an electron VDF across the shock ramp showing differences in the downstream one-dimensional cuts between weak and strong shocks. The color-coded lines indicate the different electron populations of the core (blue), halo (orange), and beam/strahl (red). The top (bottom) row show cuts parallel (perpendicular) to the local quasi-static magnetic field.

3. $0.3\% \lesssim \widetilde{\Delta\Pi}_{eb,j} \lesssim 16.5\%$;
4. $1.8\% \lesssim \widetilde{\Delta\Pi}_{{\rm eff},j} \lesssim 66.7\%$;
5. $1.8\% \lesssim \widetilde{\Delta\Pi}_{p,j} \lesssim 66.7\%$; and
6. $0.07\% \lesssim \widetilde{\Delta\Pi}_{\alpha,j} \lesssim 10.8\%$.

Therefore, the core electrons and protons both carry the largest $\Pi_{s,j}$, and they tend to experience the largest $\widetilde{\Delta\Pi}_{s,j}$.

Of the three minor partial pressure populations (i.e., halo, beam/strahl, and alpha particles), the halo electrons consistently dominate in the upstream region, especially $\Pi_{eh,\parallel}$. In the downstream, $\Pi_{eb,\perp}$ and $\Pi_{\alpha,\perp}$ can be comparable to $\Pi_{eh,\perp}$. Interestingly, the $\Pi_{ec,j}$ and $\Pi_{p,j}$ often vary out of phase with each other suggesting a partial thermal pressure balance. This is more weakly reflected in the $\Pi_{\alpha,j}$ variations relative to the $\Pi_{eh,j}$ and $\Pi_{eb,j}$ values.

Unexpectedly, it was found that the change in pressure of the electrons could be comparable to or larger than the protons. That is, the ratio of these changes for the 52 IP shocks examined herein (shown as $X_{\rm min} \lesssim X \lesssim X_{\rm max}$, $\tilde{X}$) satisfies the following:

1. $16.9\% \lesssim \widetilde{\Delta P}_{ec,j}/\widetilde{\Delta P}_{p,j} \lesssim 391\%$, $\sim$101%;
2. $1.11\% \lesssim \widetilde{\Delta P}_{eh,j}/\widetilde{\Delta P}_{p,j} \lesssim 41.3\%$, $\sim$5.41%;
3. $0.47\% \lesssim \widetilde{\Delta P}_{eb,j}/\widetilde{\Delta P}_{p,j} \lesssim 18.3\%$, $\sim$2.55%; and
4. $19.6\% \lesssim \widetilde{\Delta P}_{{\rm eff},j}/\widetilde{\Delta P}_{p,j} \lesssim 453\%$, $\sim$107%.

Therefore, the change in core electron thermal pressure is comparable to or larger than that for the protons. This is somewhat unexpected because most IP shock observations and theory suggest that the ions should gain more thermal energy than the electrons. However, previous low Mach number bow shock observations showed that the electrons gained roughly the same fraction of thermal energy as the ions. The fractional energy density gain by the electrons increases with increasing Mach number in this study, but it is unclear if the increase is influenced by difficulty of the Wind SWE Faraday cups measuring ion distributiions downstream of the strongest events.

The nonlinear trend shown in Figure 7 between $\widetilde{\Delta T_{s,j}}$ and $\Delta\overline{KE}_{\rm shn}$ is apparent "by eye," but as the lower/upper uncertainty bounds on the fit lines illustrate, the trend is moderate at best. While some previous studies examined a linear relationship between these two parameters, they were primarily focused on observations at the much higher Mach number bow shock. Further, the fits were performed and shown between these two parameters because they were the best. Virtually every combination of macroscopic shock parameters was examined against nearly every $\widetilde{\Delta Q}$, but none exhibited a good correlation except between $\Delta\bar{\xi}_{\rm shn}$ and $\widetilde{\Delta\epsilon_j}$ (not shown). However, the good correlation between $\Delta\bar{\xi}_{\rm shn}$ and $\widetilde{\Delta\epsilon_j}$ merely shows that as the available free energy increases, the total internal energy increases, which is not surprising.

The influence of the macroscopic shock parameters is not evident in the current data set. In the following, a moderate correlation shows a clear trend but a significant spread in the dependent variable for any given independent variable value (e.g., similar to $\widetilde{\Delta T_{s,j}}$ plots in Figure 7). There is a moderate, positive correlation between $\Delta\bar{U}_{\rm shn}$ and both $\widetilde{\Delta\Pi}_{eb,j}$ and $\widetilde{\Delta\Pi}_{\alpha,j}$. There are also moderate, positive correlations between $\widetilde{\Delta\Pi}_{\alpha,j}$ and both $\Delta\overline{KE}_{\rm shn}$ and $\langle M_{Te}\rangle_{\rm up}$. In summary, none of the energy density ratios showed a clear dependence upon any macroscopic shock parameter. Nothing was found to show any dependence upon $\theta_{\rm Bn}$. That is, the change in the fractional thermal energy densities of the five major particle populations appear to be independent of the shock geometry. Therefore, microscopic instabilities were investigated because they are known to affect each population differently (e.g., Sagdeev 1966; Krall & Trivelpiece 1973; Dum 1978a, 1978b; Petkaki et al. 2003, 2006; Osmane & Hamza 2012; Artemyev et al. 2013, 2014, 2015, 2016, 2017a, 2017b, 2018; Chang et al. 2013; Hughes et al. 2014).

Over 97% of the 9362 VDFs shown in Figure 6 are unstable to either the WHFI or temperature anisotropy instabilities (WTAI). Roughly ∼1% and ∼14% of the 12,081 VDFs with both ion and electron data are unstable to the firehose and mirror instabilities, respectively, which is over an order of magnitude higher the ambient solar wind estimates (e.g., Chen et al. 2016). Nearly 30% of these VDFs satisfy $\mathcal{T}^{e}_{p_{\rm tot}} \geqslant 3$—that is, the threshold below which ion acoustic waves (IAWs) are predicted to experience heavy Landau damping. However, only ∼5% of the VDFs satisfied the critical drift velocity (between electrons and ions) threshold necessary to generate current-driven IAWs ignoring temperature gradients, which reduce this threshold. Thus, there is sufficient statistical evidence of unstable VDFs near IP shocks, which is not surprising.

There are several caveats when interpreting the above instability occurrence rates. For instance, this work used three electron, one core proton, and one alpha-particle beam populations, whereas Chen et al. (2016) used one electron, two proton, and one alpha-particle beam populations. Further, the instability threshold for the WHFI and WTAI corresponds to extremely slow growth rates in excess of 18,000 electron cyclotron periods. Finally, the IAW thresholds were derived for single, isotropic Maxwellian electron, and ion populations. Thus, these instability occurrence rates are only intended to serve as zeroth order proxies of a fully kinetic treatment that includes non-Maxwellian VDFs and multi-component electron and ion populations. Despite the caveats and the sometimes unexpectedly high occurrence rates, recent fully kinetic analysis of the ion VDFs in the solar wind finds that most intervals are linearly unstable (e.g., Klein et al. 2018, 2019).

The examination of whistler and acoustic instabilities is driven by their difference in resonance energy ranges. The former tend to scatter with the suprathermal electrons affecting both $\mathcal{A}_s$ and κ_s (e.g., Saito & Gary 2007; Gary et al. 2011; Chang et al. 2013; Hughes et al. 2014), while the latter strongly scatters the core reducing $\mathcal{A}_{ec}$ and increasing s_{ec} (or p_{ec}). There is some evidence to support the differences in $\mathcal{A}_{eh}$ and $\mathcal{A}_{eb}$ combined with differences in κ_{eh} and κ_{eb} to suggest the WHFI is present and scattering the suprathermal electrons near these IP shocks. The core electron exponents (s_{ec}, p_{ec}, and q_{ec}) are consistently larger downstream than upstream, and the profile of the downstream core electrons does reach the flattop stage (i.e., $p_{ec} \geqslant 4$) in the strongest shocks. This is consistent with the nonlinear saturation stage of IAWs interacting with electrons (e.g., Vedenov 1963; Sagdeev 1966; Dum et al. 1974; Dum 1975; Dyrud & Oppenheim 2006), but it could also be due to quasi-static cross-shock electric fields (e.g., Scudder et al. 1986; Schwartz et al. 1988, 2011; Hull et al. 2001; Mitchell & Schwartz 2014; Schwartz 2014). However, the influence of both of these effects should increase with Mach number, yet the differences in core electron exponents between low and high Mach number shocks are not statistically significant. This begs the question of how much energy/momentum goes into increasing the exponent versus increasing the temperature (which does consistently and significantly change across the shocks).

7. Conclusions

The analysis of 15,210 VDFs observed by the Wind spacecraft within ±2 hr of 52 interplanetary (IP) shocks has been presented. Five primary constituent particle populations were included in the analysis, which are the electron core ($s = ec$), halo ($s = eh$), beam/strahl ($s = eb$), and proton ($s = p$) and alpha-particle ($s = \alpha$) populations. The analysis revealed that most of the VDFs are at least linearly unstable to one or more instabilities, consistent with a similar conclusion based on different techniques applied to ion data in the ambient solar wind (e.g., Klein et al. 2018, 2019). For the weaker shocks, the change in core electron, effective electron, and total ion temperature is positively correlated with the change in kinetic energy across the shock in a way that appears to be nonlinear.

The evolution of the electron VDF illustrated in Figure 10 shows the qualitative trends observed in this study. The remaining question is what controls the increase in the core exponent versus temperature and why some strong shocks seem to prefer one or the other while the strongest shocks increase both. Neither instabilities or quasi-static fields alone appear to be capable of producing the observed changes in the electron VDFs. Kinetic simulations and theoretical work are required to resolve this discrepancy and are beyond the scope of this study.

Neither instabilities or quasi-static fields alone are sufficient to explain the evolution of the electron VDFs across the IP shocks. For instance, some of the stronger shocks showed significant core electron heating but little change in the core exponent (i.e., no additional flattening) while others showed significant increases in the core exponent (i.e., strong flattening) but comparatively weak heating. Theory and

simulations have found that nonlinear stochastic acceleration by ion acoustic waves (i.e., referred to as inelastic collisions herein) can self-consistently generate flattops in the core electron VDFs, but it is not clear what fraction of the wave energy goes into increasing the exponent versus increasing the temperature. Further, previous studies have argued that quasi-static fields are capable of producing flattop VDFs, but it is not clear what exponent value should result. Both of these explanations are plagued by the fact that the downstream core electron exponents are not positively correlated with Mach number or change in kinetic energy—quantities that have been correlated with the amplitude of both the electrostatic waves and quasi-static electric fields in collisionless shocks. That is, stronger shocks do not consistently generate flatter core electron VDFs. Addressing such fundamental questions in kinetic theory are planned in future studies.

In summary, the core electrons and protons carry the most thermal energy density, and they also experience the largest changes in thermal energy density across the shocks. A moderate, positive correlation is found between $\widetilde{\Delta T}_{s,j}$ and $\Delta\overline{KE}_{\rm shn}$, for $s = ec$, eff, and i. Weaker correlations are found between some VDF parameters and any other macroscopic shock parameter, but nothing is correlated with the shock normal angle. Surprisingly, the change across the shock in core electron pressure relative to the proton pressure, $\widetilde{\Delta P}_{ec,j}/\widetilde{\Delta P}_{p,j}$, was found to be comparable to or larger than unity. That is, the core electron pressure change was larger than that of the protons in at least 23 of the 52 shocks, for all j. If only the parallel pressures are examined, the number of shocks increases to 28 of 52. Future work will further examine the kinetic physics involved in collisionless shocks to address these open questions.

The authors thank A. F.- Viñas, D. A. Roberts, and R. A. Treumann for useful discussions of basic plasma physics and C. Markwardt for helpful feedback on the usage nuances of his MPFIT software. The work was supported by the International Space Science Institute's (ISSI) International Teams programme. L.B.W. was partially supported by Wind MO&DA grants and a Heliophysics Innovation Fund (HIF) grant. L.-J.C. and S.W. were partially supported by the MMS mission in addition to NASA grants 80NSSC18K1369 and 80NSSC17K0012, NSF grants AGS-1619584 and AGS-1552142, and DOE grant DESC0016278. D.L.T. was partially supported by NASA grant NNX16AQ50G. M.L.S. was partially supported by grants NNX14AT26G and NNX13AI75G. J.C.K. was partially supported by NASA grants NNX14AR78G and 80NSSC18K0986. D.C. was partially supported by grants NNX17AG30G, GO8-19110A, 80NSSC18K1726, 80NSSC18K1218, and NSF grant 1714658. S.J.S. was partially supported by the MMS/FIELDS investigation. C.S.S. was partially supported by NASA grant NNX16AI59G and NSF SHINE grant 1622498. S.D.B. and C.S.S. were partially supported by NASA grant NNX16AP95G. S.D.B. acknowledges the support of the Leverhulme Trust Visiting Professor program. M.P.P. and K.A.G. were supported by Parker Solar Probe instrument funds.

Appendix A
Definitions and Notation

As in Papers I and II, in this appendix, the symbols and notation used throughout will be defined. In all direction-dependent parameters, we use the subscript j to represent the direction where $j = \rm tot$ for the entire distribution, $j = \parallel$ for the parallel direction, and $j = \perp$ for the perpendicular direction, where parallel/perpendicular is with respect to the quasi-static magnetic field vector, $\boldsymbol{B}_o$ (nT). The use of the generic subscript s to denote the particle species (e.g., electrons, protons, etc.) or the component of a single particle species (e.g., electron core). For the electron components, the subscript will be $s = ec$ for the core, $s = eh$ for the halo, $s = eb$ for the beam/strahl, $s = \rm eff$ for the effective, $s = \rm int$ for the integrated (see Paper II for definition), and $s = e$ for the total/entire[27] population. The symbol/parameter definitions are as follows.

1. *One-variable statistics*
   (a) $X_{\rm min}$ ≡ minimum
   (b) $X_{\rm max}$ ≡ maximum
   (c) $\bar{X}$ ≡ mean
   (d) $\tilde{X}$ ≡ median
   (e) $X_{5\%}$ ≡ 5th percentile
   (f) $X_{25\%}$ ≡ lower quartile
   (g) $X_{75\%}$ ≡ upper quartile
   (h) $X_{95\%}$ ≡ 95th percentile
   (i) σ ≡ standard deviation
   (j) σ^2 ≡ variance
2. *Fundamental parameters*
   (a) ε_o ≡ permittivity of free space
   (b) μ_o ≡ permeability of free space
   (c) c ≡ speed of light in vacuum [km s^{-1}] = $(\varepsilon_o\,\mu_o)^{-1/2}$
   (d) k_B ≡ the Boltzmann constant [J K^{-1}]
   (e) e ≡ the fundamental charge [C]
3. *Plasma parameters*
   (a) n_s ≡ the number density [cm^{-3}] of species s
   (b) m_s ≡ the mass [kg] of species s
   (c) Z_s ≡ the charge state of species s
   (d) q_s ≡ the charge [C] of species $s = Z_s\,e$
   (e) $T_{s,j}$ ≡ the scalar temperature [eV] of the jth component of species s
   (f) $P_{s,j} = n_s\,k_B\,T_{s,j}$ ≡ the partial thermal pressure [eV cm^{-3}] of the jth component of species s
   (g) $P_{t,j} = \sum_s P_{s,j}$ ≡ the total pressure [eV cm^{-3}] of the jth component, summed over all species
   (h) $\mathcal{T}_{s'\,j} = (T_{s'}/T_s)_j$ ≡ the temperature ratio [N/A] of species s and s' of the jth component
   (i) $\mathcal{A}_s = (T_\perp/T_\parallel)_s$ ≡ the temperature anisotropy [N/A] of species s
   (j) $V_{Ts,j}$ ≡ the most probable thermal speed [km s^{-1}] of a one-dimensional velocity distribution (see Equation (A1c))
   (k) $\boldsymbol{V}_{os}$ ≡ the drift velocity [km s^{-1}] of species s in the plasma bulk flow rest frame
   (l) $\xi_{s,j} = \frac{1}{2} m_s\,n_s\,V_{os,j}^2$ ≡ the ram energy density [eV cm^{-3}] of the jth component of species s in the plasma bulk flow rest frame
   (m) $\epsilon_j = \frac{B_o^2}{2\,\mu_o} + \sum_s [P_{s,j} + \xi_{s,j}]$ ≡ the total energy density [eV cm^{-3}] of the jth component of the system in the plasma bulk flow rest frame

[27] This subscript is used in previous studies and defined here as a reference. Throughout this manuscript, the use of only e will be exclusively reserved for parameters discussed in previous studies.

(n) $\zeta_{s,j} = \frac{\zeta_{s,j}}{\epsilon_j} \equiv$ the ratio of the ram energy density of the jth component of species s to the total energy density [N/A]
(o) $\psi_{s,j} = \frac{P_{s,j}}{\epsilon_j} \equiv$ the ratio of the thermal energy density (partial pressure) of the jth component of species s to the total energy density [N/A]
(p) $\Pi_{s,j} = \frac{P_{s,j}}{P_{t,j}} \equiv$ the ratio of the partial thermal pressure of the jth component of species s to the total thermal pressure [N/A]
(q) $C_s \equiv$ the sound or ion-acoustic sound speed [km s^{-1}] (see supplemental PDF file Wilson et al. 2019c, for definitions)
(r) $V_A \equiv$ the Alfvén speed [km s^{-1}] (see supplemental PDF file Wilson et al. 2019c, for definitions)
(s) $V_f \equiv$ the fast mode speed [km s^{-1}] (see supplemental PDF file Wilson et al. 2019c, for definitions)
(t) $\Omega_{cs} \equiv$ the angular cyclotron frequency [rad s^{-1}] (see Equation A1(d))
(u) $\omega_{ps} \equiv$ the angular plasma frequency [rad s^{-1}] (see Equation A1(e))
(v) $\lambda_{De} \equiv$ the electron Debye length [m] (see Equation A1(f))
(w) $\rho_{cs} \equiv$ the thermal gyroradius [km] (see Equation A1(g))
(x) $\lambda_s \equiv$ the inertial length [km] (see Equation A1(h))
(y) $\beta_{s,j} \equiv$ the plasma beta [N/A] of the jth component of species s (see Equations A1(i) and A1(j))
(z) $\kappa_s \equiv$ the kappa exponent of species s (e.g., see Wilson et al. 2019a, for definition in model fit equation)
(aa) $s_s \equiv$ the symmetric self-similar exponent of species s (e.g., see Wilson et al. 2019a, for definition in model fit equation)
(ab) $p_s(q_s) \equiv$ the parallel(perpendicular) asymmetric self-similar exponent of species s (e.g., see Wilson et al. 2019a, for definition in model fit equation)
(ac) $\phi_{sc} \equiv$ the scalar, quasi-static spacecraft potential [eV] (e.g., Pulupa et al. 2014; Scime et al. 1994) (see Appendices of Paper I for more details)
(ad) $E_{\rm min} \equiv$ the minimum energy bin midpoint value [eV] of an electrostatic analyzer (e.g., see Appendices in Wilson et al. 2017, 2018)
(ae) $q_{e,\parallel} = \frac{m_e}{2} \int d^3v\, f_e^{(\rm mod)}\, v_\parallel\, v^2 \equiv$ the parallel electron heat flux [μW m^{-2}] of the entire electron VDF model, $f_e^{(\rm mod)} = f^{(\rm core)} + f^{(\rm halo)} + f^{(\rm beam)}$
(af) $q_{eo} = \frac{3}{2}\, m_e\, n_e\, V_{Tec,\parallel}{}^3 \equiv$ the free-streaming limit electron heat flux [μW m^{-2}] (e.g., Gary et al. 1999)

Similar to Paper I, the variables that rely upon multiple parameters are given in the following equations:

$$T_{{\rm eff},j} = \frac{\sum_s n_s\, T_{s,j}}{\sum_s n_s} \tag{A1a}$$

$$T_{s,\rm tot} = \frac{1}{3}(T_{s,\parallel} + 2\, T_{s,\perp}) \tag{A1b}$$

$$V_{Ts,j} = \sqrt{\frac{2\, k_B\, T_{s,j}}{m_s}} \tag{A1c}$$

$$\Omega_{cs} = \frac{q_s\, B_o}{m_s} \tag{A1d}$$

$$\omega_{ps} = \sqrt{\frac{n_s\, {q_s}^2}{\varepsilon_o\, m_s}} \tag{A1e}$$

$$\lambda_{De} = \frac{V_{Te,\rm tot}}{\sqrt{2}\ \omega_{pe}} = \sqrt{\frac{\varepsilon_o\, k_B\, T_{e,\rm tot}}{n_e\, e^2}} \tag{A1f}$$

$$\rho_{cs} = \frac{V_{Ts,\rm tot}}{\Omega_{cs}} \tag{A1g}$$

$$\lambda_s = \frac{c}{\omega_{ps}} \tag{A1h}$$

$$\beta_{s,j} = \frac{2\mu_o n_s k_B T_{s,j}}{|\boldsymbol{B}_o|^2} \tag{A1i}$$

$$\beta_{{\rm eff},j} = \frac{2\mu_o n_{\rm eff} k_B T_{{\rm eff},j}}{|\boldsymbol{B}_o|^2}, \tag{A1j}$$

where $n_{\rm eff}$ is defined as

$$n_{\rm eff} = \sum_s n_{es}. \tag{A1k}$$

For the macroscopic shock parameters, the values are averaged over asymptotic regions away from the shock transition region.

1. *Shock parameters*
(a) subscripts up and $dn \equiv$ denote the upstream (i.e., before the shock arrives time-wise at the spacecraft for a forward shock) and downstream (i.e., the shocked region)
(b) $\langle Q\rangle_j \equiv$ the average of parameter Q over the jth shock region, where $j =$ up or dn
(c) $\Delta\bar{Q} = \langle Q\rangle_{dn}$ - $\langle Q\rangle_{\rm up} \equiv$ the change in the asymptotic average of parameter Q over the jth shock region
(d) $\bar{R}_{ns} = \langle n_s\rangle_{dn}/\langle n_s\rangle_{\rm up} \equiv$ the average shock compression ratio of species s
(e) $\bar{R}_{Qs,j} = \langle Q_{s,j}\rangle_{dn}/\langle Q_{s,j}\rangle_{\rm up} \equiv$ the downstream-to-upstream jth component ratio of the asymptotic average of parameter Q of species s
(f) $\Delta\mathcal{Q}_{\alpha,\beta} = Q_\alpha$ - $Q_\beta \equiv$ the set of all permutations of the difference between all the downstream (α) and all the upstream (β) values
(g) $\widetilde{\Delta Q} \equiv$ the median of $\Delta\mathcal{Q}_{\alpha,\beta}$ (i.e., the median value of all permutations of all differences across the shock of parameter Q)
(h) $\boldsymbol{n}_{sh} \equiv$ the shock normal unit vector [N/A]
(i) $\theta_{\rm Bn} \equiv$ the shock normal angle[28] [deg]
(j) $\langle|V_{\rm shn}|\rangle_j \equiv$ the jth region average shock normal speed [km s^{-1}] in the spacecraft frame
(k) $\langle|U_{\rm shn}|\rangle_j \equiv$ the jth region average shock normal speed [km s^{-1}] in the shock rest frame (i.e., the speed of the flow relative to the shock)
(l) $\langle|KE_{\rm shn}|\rangle_j = \frac{1}{2}\, m_p\, \langle|U_{\rm shn}|\rangle_j^2 \equiv$ the jth region average shock normal kinetic energy [eV] in the shock rest frame
(m) $\langle|\xi_{\rm shn}|\rangle_j = \frac{1}{2}\, m_p\, \langle n_p\rangle_j\, \langle|U_{\rm shn}|\rangle_j^2 \equiv$ the jth region average shock normal kinetic energy density [eV cm^{-3}] in the shock rest frame
(n) $\langle M_A\rangle_j = \langle|U_{\rm shn}|\rangle_j/\langle V_A\rangle_j \equiv$ the jth region average Alfvénic Mach number [N/A]

[28] The acute reference angle between $\langle\boldsymbol{B}_o\rangle_{\rm up}$ and $\boldsymbol{n}_{sh}$.

(o) $\langle M_f \rangle_j = \langle |U_{\rm shn}| \rangle_j / \langle V_f \rangle_j \equiv$ the *jth* region average fast mode Mach number [N/A]
(p) $\langle M_{Te} \rangle_j = \langle |U_{\rm shn}| \rangle_j / \langle V_{Teff,{\rm tot}} \rangle_j \equiv$ the *jth* region average electron thermal Mach number [N/A]
(q) $M_{cr} \equiv$ the first critical Mach number [N/A]

For brevity, the percent difference between one-variable statistics values for two different selection criteria are defined here. The percent difference between parameters satisfying *Criteria DN* and *Criteria UP* is defined as $\Delta Q_{d2u} = (Q_{dn} - Q_{\rm up})/Q_{\rm up} \times 100\%$, where Q is any one-variable statistic value. Similarly, the percent difference between *Criteria HM* and *Criteria LM* is defined as $\Delta Q_{h2l} = (Q_{HM} - Q_{LM})/Q_{LM} \times 100\%$ and that between *Criteria PE* and *Criteria PA* is $\Delta Q_{\perp 2\parallel} = (Q_{PE} - Q_{PA})/Q_{PA} \times 100\%$.

As in Paper II, integrated velocity moments refer to the velocity moments calculated by integrating over the entire model function, $f_e^{(\rm mod)} = f^{(\rm core)} + f^{(\rm halo)} + f^{(\rm beam)}$, rather than the fit values from the components. The integrated moments are only calculated for VDFs with stable solutions for all three components using the Simpson's $\frac{1}{3}$ Rule algorithm. The integrals are calculated in the core electron rest frame; thus the only relevant heat flux component is the parallel, $q_{e,\parallel}$, because the suprathermal electrons have no finite perpendicular drift velocities (e.g., see Paper I). For further details on the integrated velocity moments, see Paper II.

These definitions are used throughout.

Appendix B
Extra Statistics

In this section, some extra statistics are presented in tabular form in Tables B1 and B2.

Table B1
Component Thermal Pressure-to-total Energy Density Ratios as Percentages

Ratios	$X_{\rm min}$ [a]	$X_{5\%}$ [b]	$X_{25\%}$ [c]	$\bar{X}$ [d]	$\tilde{X}$ [e]	$X_{75\%}$ [f]	$X_{95\%}$ [g]	$X_{\rm max}$ [h]
Criteria AT: 15,210 VDFs								
$\psi_{ec,\parallel}$	4.54	15.6	25.3	35.6	32.2	46.9	61.1	94.9
$\psi_{ec,\perp}$	4.81	11.5	23.3	35.1	32.5	48.3	61.9	95.1
$\psi_{ec,{\rm tot}}$	6.02	14.3	23.8	34.0	31.4	45.3	57.5	95.1
$\psi_{eh,\parallel}$	0.007	0.72	1.70	4.10	3.27	5.32	11.0	71.1
$\psi_{eh,\perp}$	0.02	0.78	1.81	4.40	3.52	5.67	11.6	72.4
$\psi_{eh,{\rm tot}}$	0.02	0.77	1.74	4.12	3.34	5.39	10.5	72.0
$\psi_{eb,\parallel}$	0.002	0.18	0.69	2.11	1.55	2.92	5.88	17.3
$\psi_{eb,\perp}$	0.001	0.23	0.69	1.97	1.50	2.70	5.40	14.3
$\psi_{eb,{\rm tot}}$	0.001	0.21	0.70	1.93	1.47	2.68	5.11	13.7
$\psi_{{\rm eff},\parallel}$	0.09	18.0	29.4	40.9	37.5	53.8	70.5	99.4
$\psi_{{\rm eff},\perp}$	0.10	13.2	27.2	40.5	37.8	54.4	72.0	99.4
$\psi_{{\rm eff},{\rm tot}}$	0.06	16.5	27.8	39.2	36.2	50.8	66.7	99.4
$\psi_{p,\parallel}$	0.45	5.96	12.4	23.9	21.2	32.1	51.4	92.1
$\psi_{p,\perp}$	0.61	6.92	14.6	23.6	20.9	30.6	49.0	89.4
$\psi_{p,{\rm tot}}$	0.61	6.11	13.4	21.9	19.6	27.8	45.8	81.7
$\psi_{\alpha,\parallel}$	0.05	0.15	0.28	1.28	0.58	1.22	5.23	20.3
$\psi_{\alpha,\perp}$	0.01	0.12	0.27	1.74	0.81	2.47	6.07	25.9
$\psi_{\alpha,{\rm tot}}$	0.03	0.14	0.26	1.37	0.59	1.92	4.91	13.6
Criteria UP: 6546 VDFs								
$\psi_{ec,\parallel}$	4.54	14.9	26.9	37.4	33.8	49.5	62.9	86.0
$\psi_{ec,\perp}$	3.88	11.9	26.7	38.7	37.0	51.8	64.6	85.6
$\psi_{ec,{\rm tot}}$	3.34	11.6	25.9	35.9	33.6	47.4	58.9	85.7
$\psi_{eh,\parallel}$	0.02	0.98	2.96	5.54	4.62	6.92	13.3	71.1
$\psi_{eh,\perp}$	0.10	1.18	3.39	6.14	5.04	7.62	15.3	72.4
$\psi_{eh,{\rm tot}}$	0.09	1.06	3.09	5.56	4.63	6.98	13.4	72.0
$\psi_{eb,\parallel}$	0.002	0.47	1.54	3.08	2.62	4.15	7.02	17.3
$\psi_{eb,\perp}$	0.04	0.53	1.52	2.89	2.55	3.75	6.47	14.3
$\psi_{eb,{\rm tot}}$	0.02	0.50	1.48	2.78	2.49	3.65	6.03	13.5
$\psi_{{\rm eff},\parallel}$	0.12	19.8	33.0	44.7	41.5	55.6	74.2	96.8
$\psi_{{\rm eff},\perp}$	0.20	17.5	33.9	46.4	45.2	58.9	76.4	96.8
$\psi_{{\rm eff},{\rm tot}}$	0.06	18.1	32.1	43.1	41.7	52.9	68.4	96.8
$\psi_{p,\parallel}$	0.45	5.11	11.2	21.3	18.6	29.5	45.9	81.4
$\psi_{p,\perp}$	0.92	5.21	11.9	19.1	17.0	23.9	42.3	82.2
$\psi_{p,{\rm tot}}$	0.80	4.96	11.2	18.4	16.7	24.2	38.6	73.2
$\psi_{\alpha,\parallel}$	0.05	0.11	0.24	0.97	0.36	0.82	4.33	13.8
$\psi_{\alpha,\perp}$	0.05	0.10	0.21	1.13	0.43	1.28	4.96	16.8
$\psi_{\alpha,{\rm tot}}$	0.06	0.11	0.22	0.81	0.35	0.80	3.04	10.4
Criteria DN: 8664 VDFs								
$\psi_{ec,\parallel}$	4.91	16.0	24.3	34.3	31.0	43.7	58.7	94.9
$\psi_{ec,\perp}$	0.48	11.4	21.3	32.5	29.7	41.8	59.8	95.1
$\psi_{ec,{\rm tot}}$	0.60	14.7	22.6	32.6	30.1	42.5	56.2	95.1
$\psi_{eh,\parallel}$	0.007	0.63	1.39	3.06	2.41	4.06	7.45	25.0
$\psi_{eh,\perp}$	0.02	0.67	1.46	3.15	2.57	4.18	7.67	22.6
$\psi_{eh,{\rm tot}}$	0.02	0.68	1.43	3.08	2.50	4.11	7.47	23.0
$\psi_{eb,\parallel}$	0.002	0.14	0.49	1.38	1.00	1.84	3.88	16.0
$\psi_{eb,\perp}$	0.001	0.16	0.50	1.27	0.93	1.72	3.39	14.1
$\psi_{eb,{\rm tot}}$	0.001	0.16	0.51	1.29	0.94	1.73	3.34	13.7
$\psi_{{\rm eff},\parallel}$	0.09	17.7	26.8	38.0	34.6	49.7	64.7	99.4
$\psi_{{\rm eff},\perp}$	0.10	12.3	23.9	36.2	33.5	46.2	65.1	99.4
$\psi_{{\rm eff},{\rm tot}}$	0.09	16.2	25.2	36.3	33.8	47.6	62.2	99.4
$\psi_{p,\parallel}$	1.05	7.04	14.0	26.1	23.5	35.6	54.4	92.1
$\psi_{p,\perp}$	0.61	9.93	17.5	27.1	23.6	34.3	52.5	89.4
$\psi_{p,{\rm tot}}$	0.61	10.1	16.1	25.0	21.8	32.0	48.7	81.7
$\psi_{\alpha,\parallel}$	0.10	0.27	0.57	1.90	0.90	2.56	6.31	20.3
$\psi_{\alpha,\perp}$	0.01	0.19	0.69	2.62	1.96	3.84	6.85	25.9
$\psi_{\alpha,{\rm tot}}$	0.03	0.30	0.73	2.46	2.05	3.51	5.80	13.6

Notes. All values represented as percentages. For symbol definitions, see Appendix A.
[a] Minimum.
[b] 5th percentile.
[c] 25th percentile.
[d] Mean.
[e] Median.
[f] 75th percentile.
[g] 95th percentile.
[h] Maximum.

Table B2
Component-to-total Thermal Pressure Ratios as Percentages

Ratios	$X_{\min}$	$X_{5\%}$	$X_{25\%}$	$\bar{X}$	$\tilde{X}$	$X_{75\%}$	$X_{95\%}$	$X_{\max}$
Criteria AT: 15,210 VDFs								
$\Pi_{ec,\parallel}$	7.00	30.3	45.3	60.4	61.8	73.8	91.6	99.9
$\Pi_{ec,\perp}$	4.36	25.9	43.7	56.6	57.9	69.0	87.2	99.9
$\Pi_{ec,\mathrm{tot}}$	6.67	31.9	47.6	60.9	61.2	73.7	91.1	99.9
$\Pi_{eh,\parallel}$	0.02	1.36	3.12	7.01	5.39	9.12	16.3	99.4
$\Pi_{eh,\perp}$	0.05	1.39	3.26	7.27	5.71	9.45	17.0	96.8
$\Pi_{eh,\mathrm{tot}}$	0.14	1.50	3.43	7.55	5.91	9.85	17.5	97.8
$\Pi_{eb,\parallel}$	0.003	0.30	1.16	3.84	2.59	5.21	11.0	80.6
$\Pi_{eb,\perp}$	0.003	0.36	1.15	3.39	2.45	4.62	8.99	73.2
$\Pi_{eb,\mathrm{tot}}$	0.004	0.39	1.28	3.69	2.66	5.03	9.44	75.8
$\Pi_{\mathrm{eff},\parallel}$	0.15	33.8	49.6	63.4	65.9	78.1	86.6	98.9
$\Pi_{\mathrm{eff},\perp}$	0.23	29.4	48.4	61.4	65.0	75.0	85.4	97.2
$\Pi_{\mathrm{eff,tot}}$	0.19	35.3	52.6	63.7	66.0	76.2	85.4	97.8
$\Pi_{p,\parallel}$	1.09	13.3	21.6	36.4	34.0	50.3	66.3	99.9
$\Pi_{p,\perp}$	2.84	14.3	24.1	37.8	33.9	50.4	71.9	99.8
$\Pi_{p,\mathrm{tot}}$	2.17	14.4	23.3	36.0	33.2	47.3	64.6	99.8
$\Pi_{\alpha,\parallel}$	0.07	0.19	0.35	1.92	0.82	2.07	7.17	28.8
$\Pi_{\alpha,\perp}$	0.07	0.17	0.36	2.98	1.45	4.03	10.7	43.4
$\Pi_{\alpha,\mathrm{tot}}$	0.08	0.20	0.37	2.26	0.93	3.16	8.60	25.4
Criteria UP: 6546 VDFs								
$\Pi_{ec,\parallel}$	11.2	30.9	47.0	59.3	62.1	71.7	84.1	98.4
$\Pi_{ec,\perp}$	5.98	27.1	50.9	60.0	63.3	70.8	82.3	98.0
$\Pi_{ec,\mathrm{tot}}$	13.4	31.4	50.8	60.5	63.3	71.4	83.4	97.8
$\Pi_{eh,\parallel}$	0.04	1.74	4.58	9.15	7.47	11.2	21.8	99.4
$\Pi_{eh,\perp}$	0.22	1.98	5.43	9.87	8.32	11.9	21.9	96.8
$\Pi_{eh,\mathrm{tot}}$	0.20	1.95	5.18	9.86	8.19	11.9	22.4	97.8
$\Pi_{eb,\parallel}$	0.003	0.76	2.16	5.46	4.18	7.10	14.6	80.6
$\Pi_{eb,\perp}$	0.04	0.85	2.27	4.88	4.09	6.25	11.4	73.2
$\Pi_{eb,\mathrm{tot}}$	0.03	0.85	2.30	5.19	4.23	6.70	13.0	75.8
$\Pi_{\mathrm{eff},\parallel}$	0.84	39.9	56.3	68.2	73.0	81.3	87.9	98.9
$\Pi_{\mathrm{eff},\perp}$	1.49	36.6	62.9	70.0	73.3	82.0	88.0	97.2
$\Pi_{\mathrm{eff,tot}}$	1.97	39.3	62.0	69.9	73.2	81.8	87.9	97.8
$\Pi_{p,\parallel}$	1.09	11.9	18.3	32.0	27.0	43.6	61.9	99.2
$\Pi_{p,\perp}$	2.84	11.6	17.9	29.9	26.0	35.6	67.2	99.1
$\Pi_{p,\mathrm{tot}}$	2.17	11.9	18.1	30.1	26.7	37.8	62.1	98.8
$\Pi_{\alpha,\parallel}$	0.07	0.15	0.28	1.50	0.51	1.44	5.81	28.8
$\Pi_{\alpha,\perp}$	0.08	0.15	0.26	1.99	0.62	2.26	8.53	36.6
$\Pi_{\alpha,\mathrm{tot}}$	0.08	0.16	0.28	1.47	0.54	1.54	5.56	25.4
Criteria DN: 8664 VDFs								
$\Pi_{ec,\parallel}$	7.00	30.0	44.2	61.3	61.4	77.6	94.3	99.9
$\Pi_{ec,\perp}$	4.36	24.9	40.5	54.1	52.1	65.1	89.3	99.9
$\Pi_{ec,\mathrm{tot}}$	6.67	32.2	45.4	61.2	59.4	77.2	93.5	99.9
$\Pi_{eh,\parallel}$	0.02	1.19	2.61	5.45	4.20	7.08	13.1	90.7
$\Pi_{eh,\perp}$	0.05	1.13	2.64	5.40	4.29	6.78	13.4	94.4
$\Pi_{eh,\mathrm{tot}}$	0.01	1.27	2.88	5.88	4.61	7.57	14.1	93.1
$\Pi_{eb,\parallel}$	0.005	0.22	0.81	2.62	1.72	3.56	8.01	64.2
$\Pi_{eb,\perp}$	0.003	0.27	0.81	2.27	1.58	3.09	6.27	21.8

Table B2
(Continued)

Ratios	$X_{\min}$	$X_{5\%}$	$X_{25\%}$	$\bar{X}$	$\tilde{X}$	$X_{75\%}$	$X_{95\%}$	$X_{\max}$
Criteria AT: 15,210 VDFs								
$\Pi_{eb,\mathrm{tot}}$	0.004	0.28	0.92	2.57	1.81	3.50	7.07	51.1
$\Pi_{\mathrm{eff},\parallel}$	0.15	31.2	45.8	59.5	60.7	74.0	84.7	95.4
$\Pi_{\mathrm{eff},\perp}$	0.23	26.9	43.6	54.8	54.7	68.5	79.3	93.7
$\Pi_{\mathrm{eff,tot}}$	0.19	33.2	46.8	58.4	59.6	71.0	80.7	94.0
$\Pi_{p,\parallel}$	4.55	15.2	25.6	40.2	38.7	54.0	68.6	99.9
$\Pi_{p,\perp}$	6.01	20.2	30.8	44.0	42.9	55.4	73.5	99.8
$\Pi_{p,\mathrm{tot}}$	5.99	19.3	28.6	41.2	39.9	53.0	66.5	99.8
$\Pi_{\alpha,\parallel}$	0.13	0.36	0.77	2.74	1.27	3.91	8.58	28.6
$\Pi_{\alpha,\perp}$	0.07	0.26	1.38	4.40	3.40	5.92	12.2	43.4
$\Pi_{\alpha,\mathrm{tot}}$	0.23	0.45	0.99	3.81	3.21	5.21	10.1	23.2

Note. All values are represented as percentages. The header symbols are the same as in Table B1. For symbol definitions, see Appendix A.

ORCID iDs

Lynn B. Wilson, III https://orcid.org/0000-0002-4313-1970
Li-Jen Chen https://orcid.org/0000-0002-4768-189X
Shan Wang https://orcid.org/0000-0002-6783-7759
Steven J. Schwartz https://orcid.org/0000-0003-0682-2753
Drew L. Turner https://orcid.org/0000-0002-2425-7818
Michael L. Stevens https://orcid.org/0000-0002-7728-0085
Justin C. Kasper https://orcid.org/0000-0002-7077-930X
Adnane Osmane https://orcid.org/0000-0003-2555-5953
Damiano Caprioli https://orcid.org/0000-0003-0939-8775
Stuart D. Bale https://orcid.org/0000-0002-1989-3596
Marc P. Pulupa https://orcid.org/0000-0002-1573-7457
Chadi S. Salem https://orcid.org/0000-0002-6536-1531
Katherine A. Goodrich https://orcid.org/0000-0002-4288-5084

References

Agrimson, E., D'Angelo, N., & Merlino, R. L. 2001, PhRvL, 86, 5282
Aguilar-Rodriguez, E., Blanco-Cano, X., Russell, C. T., et al. 2011, JGRA, 116, A12109
Akimoto, K., Papadopoulos, K., & Winske, D. 1985, JPlPh, 34, 467
Akimoto, K., & Winske, D. 1985, JGR, 90, 12095
Allan, W., & Sanderson, J. J. 1974, PlPh, 16, 753
Artemyev, A. V., Neishtadt, A. I., Vasiliev, A. A., & Mourenas, D. 2016, PhPl, 23, 090701
Artemyev, A. V., Neishtadt, A. I., Vasiliev, A. A., & Mourenas, D. 2017a, PhRvE, 95, 023204
Artemyev, A. V., Neishtadt, A. I., Vasiliev, A. A., & Mourenas, D. 2018, JPlPh, 84, 905840206
Artemyev, A. V., Neishtadt, A. I., Vasiliev, A. A., & Zelenyi, L. M. 2015, PhRvL, 115, 155001
Artemyev, A. V., Rankin, R., & Vasko, I. Y. 2017b, JGRA, 122, 5519
Artemyev, A. V., Vasiliev, A. A., Mourenas, D., et al. 2014, GeoRL, 41, 5727
Artemyev, A. V., Vasiliev, A. A., Mourenas, D., Agapitov, O. V., & Krasnoselskikh, V. V. 2013, PhPl, 20, 122901
Ashour-Abdalla, M., & Okuda, H. 1986, JGR, 91, 6833
Auer, P. L., Kilb, R. W., & Crevier, W. F. 1971, JGR, 76, 2927
Biskamp, D., von Hagenow, K. U., & Welter, H. 1972, PhLA, 39, 351
Blasi, P., Morlino, G., Bandiera, R., Amato, E., & Caprioli, D. 2012, ApJ, 755, 121
Breneman, A., Cattell, C., Kersten, K., et al. 2013, JGRA, 118, 7654
Breneman, A., Cattell, C., Schreiner, S., et al. 2010, JGRA, 115, 8104
Cairns, I. H., & Layden, A. 2018, PhPl, 25, 082309

Cairns, I. H., & Robinson, P. A. 1992, GeoRL, 19, 2187
Caprioli, D., & Spitkovsky, A. 2014, ApJ, 783, 91
Chang, O., Gary, S. P., & Wang, J. 2013, JGRA, 118, 2824
Chen, C. H. K., Matteini, L., Schekochihin, A. A., et al. 2016, ApJL, 825, L26
Chen, L.-J., Wang, S., Wilson, L. B., III, et al. 2018, PhRvL, 120, 225101
Cohen, Z. A., Cattell, C. A., Breneman, A. W., et al. 2019, ApJ, submitted (arXiv:1909.08176)
Coroniti, F. V. 1970, JPlPh, 4, 265
Coroniti, F. V., Kennel, C. F., Scarf, F. L., & Smith, E. J. 1982, JGR, 87, 6029
Davis, L., Cattell, C. A., Wilson, L. B., III, et al. 2020, JGRA, submitted
Dum, C. T. 1975, PhRvL, 35, 947
Dum, C. T. 1978a, PhFl, 21, 945
Dum, C. T. 1978b, PhFl, 21, 956
Dum, C. T., Chodura, R., & Biskamp, D. 1974, PhRvL, 32, 1231
Dum, C. T., Marsch, E., & Pilipp, W. 1980, JPlPh, 23, 91
Dyrud, L. P., & Oppenheim, M. M. 2006, JGRA, 111, 1302
Feldman, W. C., Anderson, R. C., Bame, S. J., et al. 1983a, JGR, 88, 9949
Feldman, W. C., Anderson, R. C., Bame, S. J., et al. 1983b, JGR, 88, 96
Feldman, W. C., Asbridge, J. R., Bame, S. J., Gosling, J. T., & Zwickl, R. D. 1983c, in NASA Conf. Publication, JPL Solar Wind Five, 403
Feldman, W. C., Bame, S. J., Gary, S. P., et al. 1982, PhRvL, 49, 199
Fitzenreiter, R. J., Ogilvie, K. W., Bale, S. D., & Viñas, A. F. 2003, JGRA, 108, 1415
Fredricks, R. W., Coroniti, F. V., Kennel, C. F., & Scarf, F. L. 1970, PhRvL, 24, 994
Fredricks, R. W., Kennel, C. F., Scarf, F. L., Crook, G. M., & Green, I. M. 1968, PhRvL, 21, 1761
Fried, B. D., & Gould, R. W. 1961, PhFl, 4, 139
Fried, B. D., & Wong, A. Y. 1966, PhFl, 9, 1084
Fuselier, S. A., & Gurnett, D. A. 1984, JGR, 89, 91
Gary, S. P., Liu, K., & Winske, D. 2011, PhPl, 18, 082902
Gary, S. P., Scime, E. E., Phillips, J. L., & Feldman, W. C. 1994, JGR, 99, 23391
Gary, S. P., Skoug, R. M., & Daughton, W. 1999, PhPl, 6, 2607
Gavrishchaka, V. V., Ganguli, S. B., & Ganguli, G. I. 1999, JGR, 104, 12683
Ghavamian, P., Laming, J. M., & Rakowski, C. E. 2007, ApJ, 654, L69
Ghavamian, P., Schwartz, S. J., Mitchell, J., Masters, A., & Laming, J. M. 2014, in Microphysics of Cosmic Plasmas, ed. A. Balogh et al. (New York: Springer Science+Business Media), 557
Goodrich, K. A., Ergun, R. E., Schwartz, S. J., et al. 2018, JGRA, 123, 9430
Goodrich, K. A., Ergun, R. E., Schwartz, S. J., et al. 2019, JGRA, 124, 1855
Gosling, J. T., Bame, S. J., McComas, D. J., et al. 1993, GeoRL, 20, 2789
Gould, R. W. 1964, PhRv, 136, 991
Gurnett, D. A., & Anderson, R. R. 1977, JGR, 82, 632
Gurnett, D. A., & Bhattacharjee, A. 2005, Introduction to Plasma Physics: With Space and Laboratory Applications (Cambridge: Cambridge Univ. Press)
Gurnett, D. A., Marsch, E., Pilipp, W., Schwenn, R., & Rosenbauer, H. 1979a, JGR, 84, 2029
Gurnett, D. A., Neubauer, F. M., & Schwenn, R. 1979b, JGR, 84, 541
Harten, R., & Clark, K. 1995, SSRv, 71, 23
Hobara, Y., Balikhin, M., Krasnoselskikh, V., Gedalin, M., & Yamagishi, H. 2010, JGRA, 115, 11106
Horaites, K., Boldyrev, S., Wilson, L. B., III, Viñas, A. F., & Merka, J. 2018, MNRAS, 474, 115
Hughes, R. S., Gary, S. P., & Wang, J. 2014, GeoRL, 41, 8681
Hull, A. J., Scudder, J. D., Fitzenreiter, R. J., et al. 2000, JGR, 105, 20957
Hull, A. J., Scudder, J. D., Larson, D. E., & Lin, R. 2001, JGR, 106, 15711
Kasper, J. C., Lazarus, A. J., Steinberg, J. T., Ogilvie, K. W., & Szabo, A. 2006, JGRA, 111, 3105
Kasper, J. C., Maruca, B. A., Stevens, M. L., & Zaslavsky, A. 2013, PhRvL, 110, 091102
Kellogg, P. J. 1962, JGR, 67, 3805
Kellogg, P. J., Goetz, K., Monson, S. J., & Opitz, A. 2013, JGRA, 118, 4766
Kennel, C. F., Edmiston, J. P., & Hada, T. 1985, in Collisionless Shocks in the Heliosphere: A Tutorial Review, ed. R. G. Stone & B. T. Tsurutani (Washington, DC: American Geophysical Union), 1
Klein, K. G., Alterman, B. L., Stevens, M. L., Vech, D., & Kasper, J. C. 2018, PhRvL, 120, 205102
Klein, K. G., Kasper, J. C., Korreck, K. E., & Stevens, M. L. 2017, JGRA, 122, 9815
Klein, K. G., Martinović, M., Stansby, D., & Horbury, T. S. 2019, ApJ, 887, 8
Krall, N. A., & Trivelpiece, A. W. 1973, Principles of Plasma Physics (Tokyo: McGraw-Hill)
Kurth, W. S., Gurnett, D. A., & Scarf, F. L. 1979, JGR, 84, 3413
Lazar, M., Kim, S., López, R. A., et al. 2018, ApJL, 868, L25
Lazar, M., López, R. A., Shaaban, S. M., Poedts, S., & Fichtner, H. 2019, Ap&SS, 364, 171
Lazar, M., Pierrard, V., Shaaban, S. M., Fichtner, H., & Poedts, S. 2017, A&A, 602, A44
Lazar, M., Poedts, S., & Michno, M. J. 2013, A&A, 554, A64
Lazar, M., Poedts, S., & Schlickeiser, R. 2014, JGRA, 119, 9395
Lazar, M., Yoon, P. H., & Schlickeiser, R. 2012, PhPl, 19, 122108
Lee, S.-Y., Lee, E., & Yoon, P. H. 2019, ApJ, 876, 117
Lemons, D. S., & Gary, S. P. 1978, JGR, 83, 1625
Lengyel-Frey, D., Farrell, W. M., Stone, R. G., Balogh, A., & Forsyth, R. 1994, JGR, 99, 13325
Lengyel-Frey, D., Hess, R. A., MacDowall, R. J., et al. 1996, JGR, 101, 27555
Lepping, R. P., Acũna, M. H., Burlaga, L. F., et al. 1995, SSRv, 71, 207
Lin, R. P., Anderson, K. A., Ashford, S., et al. 1995, SSRv, 71, 125
Livadiotis, G. 2015, JGR, 120, 1607
López, R. A., Shaaban, S. M., Lazar, M., et al. 2019, ApJL, 882, L8
Maksimovic, M., Pierrard, V., & Riley, P. 1997, GeoRL, 24, 1151
Maksimovic, M., Zouganelis, I., Chaufray, J.-Y., et al. 2005, JGRA, 110, 9104
Maruca, B. A., Kasper, J. C., & Gary, S. P. 2012, ApJ, 748, 137
Masters, A., Schwartz, S. J., Henley, E. M., et al. 2011, JGRA, 116, A10107
Mazelle, C., Lembège, B., Morgenthaler, A., et al. 2010, in AIP Conf. Proc. 1216, Twelfth Int. Solar Wind Conf. (Melville, NY: AIP), 471
Mitchell, J. J., & Schwartz, S. J. 2014, JGRA, 119, 1080
Neubauer, F. M., & Musmann, G. 1977, JGR, 82, 3201
Ogilvie, K. W., Chornay, D. J., Fritzenreiter, R. J., et al. 1995, SSRv, 71, 55
Oka, M., Otsuka, F., Matsukiyo, S., et al. 2019, ApJ, 886, 11
Oka, M., Wilson, L. B., III, Phan, T. D., et al. 2017, ApJL, 842, L11
Osmane, A., & Hamza, A. M. 2012, PhRvE, 85, 056410
Park, J., Caprioli, D., & Spitkovsky, A. 2015, PhRvL, 114, 085003
Park, J., Ren, C., Workman, J. C., & Blackman, E. G. 2013, ApJ, 765, 147
Petkaki, P., Freeman, M. P., Kirk, T., Watt, C. E. J., & Horne, R. B. 2006, JGRA, 111, 1205
Petkaki, P., Watt, C. E. J., Horne, R. B., & Freeman, M. P. 2003, JGRA, 108, 1442
Pierrard, V., Lazar, M., Poedts, S., et al. 2016, SoPh, 291, 2165
Priest, E. R., & Sanderson, J. J. 1972, PlPh, 14, 951
Pulupa, M. P., Bale, S. D., Salem, C., & Horaites, K. 2014, JGRA, 119, 647
Rodriguez, P., & Gurnett, D. A. 1975, JGR, 80, 19
Sagdeev, R. Z. 1966, RvPP, 4, 23
Sagdeev, R. Z., Shapiro, V. D., Shevchenko, V. I., & Szego, K. 1987, JGR, 92, 1131
Saito, S., & Gary, S. P. 2007, JGRA, 112, 6116
Saito, S., Nariyuki, Y., & Umeda, T. 2017, PhPl, 24, 072304
Schwartz, S. J. 2014, JGRA, 119, 1507
Schwartz, S. J., Henley, E., Mitchell, J., & Krasnoselskikh, V. 2011, PhRvL, 107, 215002
Schwartz, S. J., Thomsen, M. F., Bame, S. J., & Stansberry, J. 1988, JGR, 93, 12923
Scime, E. E., Phillips, J. L., & Bame, S. J. 1994, JGR, 99, 14769
Scudder, J. D., Mangeney, A., Lacombe, C., Harvey, C. C., & Wu, C. S. 1986, JGR, 91, 11075
Scudder, J. D., & Olbert, S. 1979, JGR, 84, 6603
Shaaban, S. M., & Lazar, M. 2020, MNRAS, 492, 3529
Shaaban, S. M., Lazar, M., & Poedts, S. 2018, MNRAS, 480, 310
Shaaban, S. M., Lazar, M., Yoon, P. H., & Poedts, S. 2019a, ApJ, 871, 237
Shaaban, S. M., Lazar, M., Yoon, P. H., Poedts, S., & López, R. A. 2019b, MNRAS, 486, 4498
Shu, F. H. 1992, Physics of Astrophysics, Vol. II (Mill Valley, CA: Univ. Science Books)
Štverák, V., Maksimovic, M., Trávníček, P. M., et al. 2009, JGRA, 114, 5104
Tao, J., Wang, L., Zong, Q., et al. 2016a, ApJ, 820, 22
Tao, J., Wang, L., Zong, Q., et al. 2016b, in AIP Conf. Ser. 1720 (Melville, NY: AIP), 070006
Thomsen, M. F., Gosling, J. T., Bame, S. J., & Mellott, M. M. 1985, JGR, 90, 137
Thomsen, M. F., Gosling, J. T., Onsager, T. G., & Russell, C. T. 1993, JGR, 98, 3875
Thomsen, M. F., Stansberry, J. A., Bame, S. J., Gosling, J. T., & Mellott, M. M. 1987, JGR, 92, 10119
Tidman, D. A., & Krall, N. A. 1971, Shock Waves in Collisionless Plasmas (New York: Wiley)
Tong, Y., Vasko, I. Y., Artemyev, A. V., Bale, S. D., & Mozer, F. S. 2019, ApJ, 878, 41
Treumann, R. A. 2009, A&ARv, 17, 409
Trotta, D., & Burgess, D. 2019, MNRAS, 482, 1154
Vedenov, A. A. 1963, JNuE, 5, 169
Verscharen, D., Klein, K. G., Chandran, B. D. G., et al. 2018, JPlPh, 84, 905840403

Verscharen, D., Klein, K. G., & Maruca, B. A. 2019, LRSP, 16, 5
Wilson, L. B., III 2016, in Low-frequency Waves in Space Plasmas, ed. A. Keiling, D.-H. Lee, & V. Nakariakov (Washington, DC: American Geophysical Union), 269
Wilson, L. B., III, Cattell, C., Kellogg, P. J., et al. 2007, PhRvL, 99, 041101
Wilson, L. B., III, Cattell, C. A., Kellogg, P. J., et al. 2009, JGRA, 114, 10106
Wilson, L. B., III, Cattell, C. A., Kellogg, P. J., et al. 2010, JGRA, 115, 12104
Wilson, L. B., III, Chen, L.-J., Wang, S., et al. 2019a, ApJS, 243, 8
Wilson, L. B., III, Chen, L.-J., Wang, S., et al. 2019b, ApJS, 245, 24
Wilson, L. B., III, Chen, L.-J., Wang, S., et al. 2019c, Supplement to: Electron Energy Partition Across Interplanetary Shocks, 1.0, Zenodo, doi:10.5281/zenodo.2875806
Wilson, L. B., III, Chen, L.-J., Wang, S., et al. 2020, Supplement to: Electron Energy Partition Across Interplanetary Shocks: III. Analysis, 1.0, Zenodo, doi:10.5281/zenodo.3627284
Wilson, L. B., III, Koval, A., Szabo, A., et al. 2012, GeoRL, 39, 8109
Wilson, L. B., III, Koval, A., Szabo, A., et al. 2013, JGRA, 118, 5
Wilson, L. B., III, Koval, A., Szabo, A., et al. 2017, JGRA, 122, 9115
Wilson, L. B., III, Sibeck, D. G., Breneman, A. W., et al. 2014a, JGRA, 119, 6455
Wilson, L. B., III, Sibeck, D. G., Breneman, A. W., et al. 2014b, JGRA, 119, 6475
Wilson, L. B., III, Sibeck, D. G., Turner, D. L., et al. 2016, PhRvL, 117, 215101
Wilson, L. B., III, Stevens, M. L., Kasper, J. C., et al. 2018, ApJS, 236, 41
Winske, D., Giacalone, J., Thomsen, M. F., & Mellott, M. M. 1987, JGR, 92, 4411
Wu, C. S. 1984, JGR, 89, 8857
Zakharov, V. E. 1972, Sov. Phys.–JETP, 35, 908
Zakharov, V. E., & Rubenchik, A. M. 1972, JAMTP, 13, 669